JGR Solid Earth

RESEARCH ARTICLE
10.1029/2020JB020202

Compactive Deformation of Sandstone Under Crustal Pressure and Temperature Conditions

Mark Jefferd[1,2], Nicolas Brantut[1], Philip G. Meredith[1], Thomas M. Mitchell[1], and Oliver Plümper[2]

[1]Department of Earth Sciences, University College London, London, UK, [2]Department of Earth Sciences, Utrecht University, Utrecht, The Netherlands

Key Points:

- Increase in temperature to 150°C lowers both yield stress and absolute strength of sandstone
- The weakening is greater in the ductile regime than in the brittle regime
- A lowering of the fracture toughness can explain the observed weakening

Correspondence to:
M. Jefferd,
mark.jefferd.11@ucl.ac.uk

Citation:
Jefferd, M., Brantut, N., Meredith, P. G., Mitchell, T. M., & Plümper, O. (2021). Compactive deformation of sandstone under crustal pressure and temperature conditions. *Journal of Geophysical Research: Solid Earth*, *126*, e2020JB020202. https://doi.org/10.1029/2020JB020202

Received 16 MAY 2020
Accepted 14 JAN 2021

Abstract The transition from macroscopically brittle to macroscopically ductile deformation in porous sandstones is known to be pressure dependent, with compactive, ductile behavior occurring only once significant effective pressures have been reached. Within the crust, such effective pressures are associated with burial depths in the range 0.5–6 km, where the temperature is likely 35°C–200°C. To test the importance of such elevated temperature on the strength and deformability of sandstone, a series of constant strain rate, triaxial deformation experiments were performed on three different water saturated sandstones at either ambient temperature or 150°C. For each sandstone, an effective pressure range was used which spanned both the brittle and ductile deformation regimes, up to a maximum of 120 MPa. In the brittle regime, we observed a temperature-dependent lowering of the yield stress of between 8% and 17%. Within the ductile regime, we observed an even greater reduction in the yield stress of between 9% and 37%. A further notable observation is that the transition from dilatant, brittle behavior to compactive, ductile behavior tends to occur at a lower effective pressure at elevated temperature. The weakening observed at elevated temperature can be explained by a reduction in fracture toughness, which is shown mathematically to cause greater weakening in the ductile regime than in the brittle regime. The apparent reduction in fracture toughness at elevated temperature is potentially driven by a combination of a reduction in surface energy and, to a minor extent, an increase in subcritical crack growth rate.

1. Introduction

The inelastic deformation of porous sandstone under applied stress depends on the local physical and chemical environment (e.g., Baud et al., 2000). The underlying deformation mechanisms can typically be grouped into those corresponding either to the macroscopically brittle regime or the macroscopically ductile regime (Bemabe & Brace, 1990; Bésuelle et al., 2003; Wong et al., 1997; Wong & Baud, 2012). The two regimes are primarily delineated by the macroscopic volumetric change observed during deformation. The brittle regime is often associated with an overall increase in volume due to dilatant cracking, whereas the ductile regime is associated with an overall decrease in volume as a result of compaction, grain crushing and cataclastic flow. In nature, geological structures commonly exhibit deformation features that are characteristic of both regimes. For example, joints and faults are representative of localized dilatancy that occurs in the brittle regime (Aydin & Johnson, 1983), while compaction bands are an example of localized compaction structures that can result from grain crushing in the ductile regime (Mollema & Antonellini, 1996). Similar structures can be formed in laboratory experiments, and it has been demonstrated that the transition from macroscopically brittle behavior to macroscopically ductile behavior is highly dependent on the effective confining pressure (Handin et al., 1963; Wong & Baud, 2012; Wong et al., 1997).

Sandstone compaction is a phenomenon that has implications for many tectonophysical and geo-engineering applications, including fault mechanics, the earthquake cycle, reservoir productivity and reservoir management. Field measurements have shown that permeability reduction by several orders of magnitude as well as development of permeability anisotropy can result from the evolution of sandstone compaction structures (Fossen et al., 2007; Sternlof et al., 2006). These observations are complemented by results from laboratory experiments, which have shown that sandstone compaction can lead to a reduction in permeability of up to three orders of magnitude (Baud et al., 2012; Fortin et al., 2005; Zhu & Wong, 1997). The direct implications of the volume reduction associated with sandstone compaction can be observed above and

Table 1
Porosity, Mean Grain Diameter and Major Constituents of Bleursville, Locharbriggs, and Boise Sandstones

Sandstone	Initial porosity (%)	Grain size (mm)	Major constituents
Bleursville	22.7 ($x \pm 1.5$)	0.12	Quartz (66%), K-feldspar (28%), clays (4%) and mica (2%) (Heap et al., 2015)
Locharbriggs	24.3 ($x \pm 0.5$)	0.20	Quartz (88%) and K-Feldspar (6%) (Mair et al., 2000)
Boise	32.3 ($x \pm 0.5$)	0.27	Quartz (41%), Na-Feldspar (29%), K-Feldspar (22%) and clay (6%) (XRD from Kocurek Industries)

around siliciclastic reservoirs, where the removal of pore fluid can lead to elastic and inelastic compaction of the host rock (Teufel et al., 1991), leading to potential surface subsidence and seismicity.

The transition from the brittle to the ductile regime is pressure sensitive and is also a function of the grain size, porosity and rock composition (Wong & Baud, 2012). For example, Boise sandstone has an initial porosity of 35%, and macroscopic ductility is observed at effective pressures close to 5 MPa (Zhu & Wong, 1997) (and data shown in this study). Whereas for lower porosity sandstones the transition will occur at much higher effective pressures. For example, for Darley Dale sandstone with an initial porosity of 14% the transition commences at effective pressures closer to 100 MPa (Wong et al., 1997). Given the average density of crustal rocks, and assuming they are saturated with water, these transition pressures correspond to a depth range of between about 0.5 and 6 km. Taking an average geothermal gradient of 30°C km^{-1} for the upper crust (Chapman, 1986), then the temperature at these depths ranges from 35°C to 200°C. However, there is currently a paucity of laboratory data exploring the effects of elevated temperature on sandstone deformation. The limited amount of previous work available in the brittle regime suggests that a temperature increase from ambient to 70°C can reduce the failure strength of sandstone by up to 9% (Heap, Baud, & Meredith, 2009). To our knowledge, there is no systematic data set on the effect of temperature on sandstone deformation in the compactive regime. Studies on unconsolidated quartz sand have shown that under triaxial stress conditions, a temperature increase caused a weakening only in the compactive regime, where the hydrostatic grain crushing pressure, P^*, was reduced by approximately 10% when the temperature was increased from ambient temperature to 170°C (Choens & Chester, 2018; Karner et al., 2008). In contrast, the brittle regime remained essentially unaffected (Karner et al., 2008). While these insights are useful, cemented and lithified sandstones are expected to behave differently from uncemented and unlithified sand aggregates (e.g., Hangx & Brantut, 2019). Thus, there remains a need to investigate the deformation behavior of porous sandstones under the elevated temperature and pressure conditions prevailing in the upper crust. Here, we report results from triaxial deformation experiments on three porous sandstones at temperatures from ambient to 150°C and effective confining pressures from 5 to 120 MPa.

2. Sample Materials

Three sandstones of different porosity, grain size and composition were used in this study. Their key properties are presented in Table 1. Bleursville sandstone from Bleurville, Vosges, north-eastern France, is a pale beige colored sandstone with reasonably high amounts of feldspar (28%) and clay (4%) in addition to quartz (66%). Its grains are spherical to sub-spherical and have a fairly uniform diameter of about 0.12 mm, and only the faintest trace of sedimentary bedding is visible. Previous studies on this material have shown that it develops compaction bands at effective pressures above about 60 MPa (Baud et al., 2015; Fortin et al., 2005; Heap et al., 2015). Locharbriggs sandstone is a relatively homogeneous, reddish sandstone from Dumfries, south-west Scotland, with a high quartz content of 88%. Its grains are spherical, with a mean diameter of around 0.2 mm. This material has been shown to produce deformation bands due to grain crushing in both nature and in the laboratory (Mair et al., 2000). Samples of Locharbriggs sandstone show thin, sub millimetric dark bands, which are separated by several centimeters from one another. These bands run continuously through the larger 30 × 25 × 20 cm block from which the samples were cored from and the flat and linear nature of these bands suggests that they are depositional features and not naturally formed deformation beds. In the micrograph shown in Figure 1 (highlighted by red ellipse) such bands can be seen to represent areas where the grain diameter has been reduced from about 0.2 mm to ~0.08 mm. Finally, Boise sandstone from Idaho, USA, is considerably more heterogeneous than the other two sandstones, with a more varied

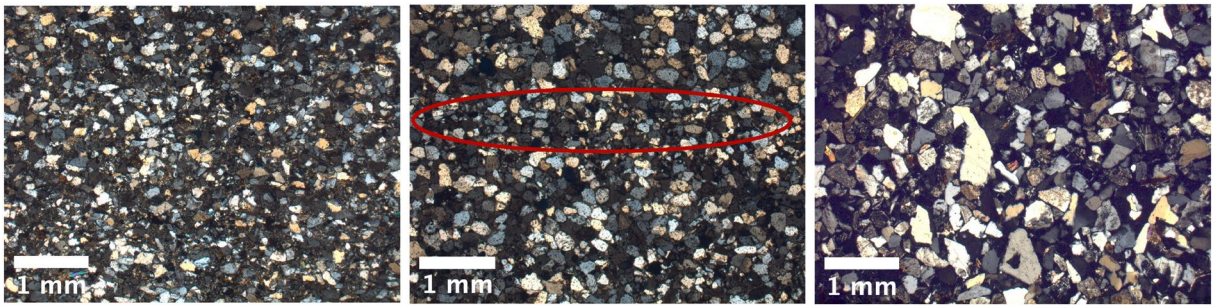

Figure 1. Micrograph images of undeformed sample of Bleursville (left), Locharbriggs (center), and Boise (right). The red ellipse in the center image highlights a region of Locharbriggs sandstone where the grain diameter is smaller by a factor of about two, which corresponds to sub-millimeter dark bands present in the undeformed Locharbriggs samples.

grain size and a less regular grain shape. While the mean grain diamter is 0.27 mm (Table 1), Boise sandstone also contains larger grains of a millimeter or more in diameter distributed throughout the rock.

Cylindrical samples of 25 mm in diameter and with lengths in the range of 51–53 mm were cored from a single block of each material, perpendicular to any sedimentary bedding, and their ends ground flat and parallel to within ≤0.1 mm. Each sample was then oven dried at 60°C for a minimum of 48 h.

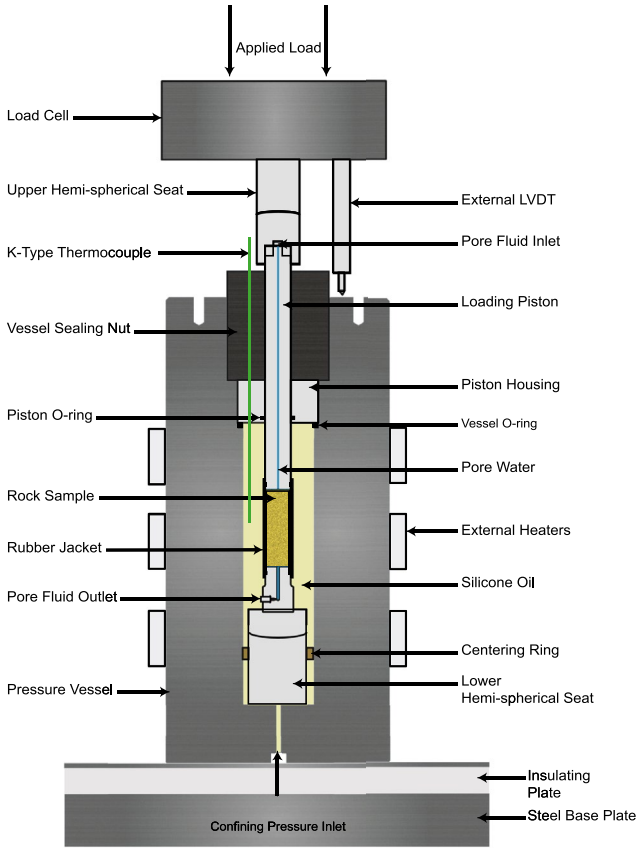

Figure 2. Schematic diagram of the triaxial deformation apparatus used in this study.

3. Experimental Apparatus

All experiments in this study were carried out using a conventional triaxial deformation apparatus in the Rock and Ice Physics Laboratory at University College London. The apparatus comprises a 200 MPa capacity pressure vessel mounted in a servo-hydraulically controlled 260 tonne loading frame (Figure 2). Confining pressure is provided to the vessel by means of a servo-controlled intensifier that uses silicone oil to provide confining pressure up to a maximum of 120 MPa. A second servo-controlled intensifier provides pore fluid pressure to the sample at up to 70 MPa. The changes in pore fluid volume, at constant pore fluid pressure, can also be monitored throughout each experiment by means of a linear variable differential transformer (LVDT) coupled to the intensifier piston. Both intensifiers are capable of maintaining a constant set pressure to a precision of ±0.1 MPa for the complete experiment duration.

The pressure vessel is fitted with three external band heaters which can raise the temperature of the vessel and the enclosed sample assembly to a maximum of 200°C. Internal temperature is measured by a thermocouple located within the confining oil close to the sample. During experiments, the oil temperature does not fluctuate from the desired set point by more than 1°C and, due to thermal inertia, the variation in the sample temperature is less than this. Calibration tests, performed by measuring the temperature along the length of a hole drilled along the central axis of a dummy sample, confirmed that the temperature varied by less than 1°C along the sample length, equivalent to a thermal gradient of less than $0.2°C\,cm^{-1}$.

Axial stress is applied to the sample via the loading ram mounted in the cross-head of the loading frame. This can be operated in one of two standard servo-controlled modes; (1) constant strain rate mode, where an external LVDT is used to impose a constant rate of displacement (compensated for the deformation of the loading train), and the applied load is measured by an external load cell (compensated for seal friction), or

(2) constant stress (creep) mode, where the load cell is used to maintain a pre-determined stress and the LVDT is used to record the corresponding axial strain as a function of time. The axial stress measured by the load cell is a combination of the maximum principal stress (σ_1) imposed on the sample and the confining pressure (P_c) within the vessel. In all our experiments, the samples were loading axisymmetrically, so that $P_c = \sigma_2 = \sigma_3$, and we use the Terzaghi effective pressure (P_{eff}) so that $P_{eff} = P_c - P_p$, where P_p is the pore fluid pressure within the sample. The differential stress, Q, is therefore simply $\sigma_1 - P_c$, and the effective mean stress, P, is given by $(\sigma_1 + 2\sigma_3)/3 - P_p$ or, equivalently, $Q/3 + P_{eff}$.

The stiffness of the loading column was determined by elastically deforming a steel sample of known length and Young's modulus, and subtracting the calculated shortening of the steel sample from the total measured shortening of the steel sample and loading column over a range of applied loads. The stiffness of the loading system, calculated in this way, was 218 kN mm^{-1}, and this value did not change with either change in confining pressure or change in temperature up to 200°C.

4. Experimental Procedure

Prior to each experiment, the oven dried sample was submerged in distilled water under vacuum for at least 2 h to saturate. The saturated sample was then inserted into a rubber jacket which was then slid over the upper and lower pistons to provide a seal against ingress of the confining fluid (Figure 2). To start an experiment, the sample assembly was inserted into the pressure vessel and the sealing nut tightened. Confining pressure was then applied, initially by means of a hand pump to a value of 8 MPa, which was then maintained by the servo-controlled intensifier. A pore pressure of 5 MPa was then applied by the pore pressure intensifier at a rate of 0.05 MPa s^{-1} and the sample allowed to fully saturate at this pressure; saturation was considered complete when the intensifier volume ceased to change. Note, if an experiment's target effective pressure was 5 MPa then the initial pore pressure was applied and increased before the confining pressure reached 5 MPa to ensure the sample was not precompacted at a higher stress than the experimental conditions. The confining pressure was then increased to the desired experimental value at a rate of 0.05 MPa s^{-1}, and left for a minimum of 2 h to achieve pressure equilibrium.

For elevated temperature experiments, the external heaters were switched on prior to the final increase in confining pressure. It took a little over 5 h for the system to reach equilibrium at a temperature of 150°C, corresponding to an average heating rate of approximately 0.5°C min^{-1}. The sample was then deformed at a constant strain rate of 1×10^{-5} s^{-1} until either brittle failure occurred or 5% axial strain was reached, at which point the experiment was stopped. The differential stress was removed slowly, at the same rate as during loading. Confining pressure was then reduced to 10 MPa, again at a rate of 0.05 MPa s^{-1}. For elevated temperature tests, the furnaces were then switched off and the vessel assembly allowed to cool to ambient temperature (taking, on average, about 10 h). Once ambient temperature was achieved, the pore pressure was decreased to zero, followed by the remaining confining pressure. The sample was then removed from the pressure vessel.

In addition to the above triaxial deformation tests, a hydrostatic loading test was also performed on each of the sandstones at both ambient temperature and at 150°C, in order to determine the grain crushing pressure, P^*, where that was feasible. This was achieved through incrementally increasing the confining pressure in small steps and observing the consequential change in pore volume. The confining pressure step size was initially 5 MPa, and this was reduced to 2 MPa as the expected P^* value was approached. For each step increase in confining pressure, the pore volume decreased due to compaction of the pore space. The compaction continued for some time after the step increase in confining pressure, so the subsequent step in confining pressure was only applied once the decrease in pore volume had ceased. The value of P^* was determined from the inflexion in the "hydrostat"; the plot of effective mean stress against porosity change. Beyond P^* the reduction in pore volume per unit of effective mean stress increases significantly due to grain crushing.

Microstructural characterization of selected samples post deformation was carried out using a Zeiss GEMINI 450 scanning electron microscope (SEM) using dual-channel secondary electron (SE) and backscattered electron (BSE) imaging. The Zeiss ATLAS software was used to obtain whole thin section scale SEM images with a resolution of 500 nm/pixel. The acceleration voltage was set to 20 kV at a beam current of 2 nA.

5. Results

In order to span both the brittle and ductile regimes for each o1f the three rocks, we conducted experiments over a range of effective pressures from 5 to 120 MPa on Bleursville sandstone, from 5 to 100 MPa on Locharbriggs sandstone, and from 5 to 35 MPa on Boise sandstone. For each value of effective pressure on each sandstone, an experiment was carried out at ambient temperature (nominally 20°C) and at 150°C. We first present stress-strain and porosity change results from experiments typical of each regime for each rock type to highlight their differences and similarities. We then present porosity change data as a function of effective mean stress for all effective confining pressures tested to highlight the transition from brittle to ductile behavior. A summary of all the experiments, with their test conditions and key results is presented in Table 2.

Results from constant strain rate experiments on Bleursville sandstone at effective pressures of 5–100 MPa, and at temperatures of 20°C–150°C are given in Figure 3, where both differential stress and porosity change are plotted against axial strain. At an effective pressure of 5 MPa, we observe typical brittle behavior. The initial concave upwards parts of the stress-strain curves are followed by quasi-linear portions from around 0.25%–0.75% axial strain. The curves then deviate from linearity and roll over to peak stress; occurring at 51 MPa at 20°C and 46 MPa at 150°C (a decrease of around 10%). With further axial strain, a phase of strain weakening is seen, which continues until macroscopic failure along shear faults oriented ∼30° to the compression axis. For the same experiments we observe an initial reduction in porosity, by 0.15% for the 20°C test and 0.1% for the 150°C test. The samples then undergo a porosity increase (or dilation) when the axial strain exceeds about 0.75%, corresponding to the point where the strain-curves deviate from linearity. By the time that macroscopic failure occurs, the samples exhibits net porosity increases of 0.6% and 0.5% for 20°C and 150°C, respectively (i.e. an increase in porosity from 22.7% to 23.3% and 23.2%). By contrast, at an effective pressure of 100 MPa we observe behavior that is typical of the ductile regime. The stress-strain behavior beyond the initial quasi-linear phase is marked by brief plateaux, occurring at a differential stress of 97 MPa at 20°C and 77 MPa at 150°C, a decrease of around 20%. These stress plateaux are indicative of cataclastic flow and last for approximately 0.5% axial strain. They are followed by phases of strain hardening that continue until the experiments are terminated at 5% axial strain. Following an initial settling-in phase, the porosity at this effective pressure decreases linearly with increasing axial strain for the remainder of both experiments, with overall reductions of 3.2% and 3.5% at 20°C and 150°C, respectively.

Qualitatively, the behavior of Locharbriggs sandstone, deformed under the same effective pressure and temperature conditions, is broadly similar to that of Bleursville sandstone, and the results are illustrated in Figure 4. At an effective pressure of 5 MPa, the samples of Locharbrigss sandstone exhibited a similar pattern of brittle deformation with the peak stress occurring at 62 MPa and 50 MPa for tests at 20°C and 150°C, respectively, which represents a reduction of 18% at elevated temperature. Prior to failure, both samples exhibited a net porosity increase of around 0.7%. For the tests carried out at an effective pressure of 100 MPa, the stress-strain behavior is very similar to that of Bleursville sandstone for the first 1% of axial strain, but with peak stresses of 131 and 111 MPa, for temperatures of 20°C and 150°C, respectively. Following these peak stresses, rather than the stress plateaux observed for Bleursville sandstone, we see stress drops of 10–20 MPa, followed by recovery. After recovery, the stress is then seen to fluctuate rather than strain harden in a uniform manner. The change in porosity of Locharbriggs sandstone follows a very similar pattern to that of Bleursville sandstone at the same effective pressure. Porosity decreases linearly with increasing axial strain throughout the duration of both experiments, accumulating total reductions of around 3.5% at both temperatures after 5%–6% strain (Figure 4d). We also note that there do not appear to be any discernible fluctuations in the porosity change curves associated with the stress drops that are clearly seen in the stress-strain curves (Figure 4b).

By comparison with Bleursville and Locharbriggs sandstones, the stress-strain behavior of Boise sandstone deformed at an effective pressure of 5 MPa is qualitatively different, as shown in Figure 5a. Boise sandstone does not exhibit an extended period of strain weakening before the peak stress, neither does it exhibit a significant stress drop at failure. It is also much weaker than either of the other two sandstones, with peak stresses of 22 and 19 MPa at 20°C and 150°C, respectively; corresponding to a decrease of 12% at the higher temperature. The change in porosity of Boise sandstone during deformation at $P_{\text{eff}} = 5$ MPa is also different from that of the other two sandstones, as illustrated in Figure 5c. This material exhibits compaction

Table 2
Summary of Experimental Conditions and Results

P_{eff} (MPa)	Temperature (°C)	Diff. Stress at C' (MPa)	Diff. Stress at C^* (MPa)	Reduction in diff. Stress at yield at 150°C (%)	Peak stress or cataclastic flow stress (MPa)	Reduction in peak stress or cataclastic flow stress at 150°C (%)
Bleursville						
5	20	18	–	–	45	–
5	150	15	–	17	51	11
20	20	39	–	–	84	–
20	150	36	–	8	64	24
25	20	–	57	–	81	–
25	150	–	45	21	74	9
35	20	–	60	–	94	–
35	150	–	51	15	82	13
55	20	–	78	–	107	–
55	150	–	57	27	87	18
80	20	–	81	–	101	–
80	150	–	54	33	81	19
100	20	–	63	–	97	–
100	150	–	48	24	77	20
120	20	–	57	–	93	–
120	150	–	36	37	66	30
Locharbriggs						
5	20	33	–	–	62	–
5	150	30	–	9	49	20
25	20	84	–	–	105	–
25	150	–	69	18	99	3
55	20	–	96	–	133	–
55	150	–	87	9	122	8
80	20	–	90	–	133	–
80	150	–	75	17	125	6
100	20	–	93	–	131	–
100	150	–	72	23	111	15
Boise						
5	20	–	14	–	22	–
5	150	–	11	23	19	12
20	20	–	12	–	22	–
20	150	–	9	25	19	10
30	20	–	11	–	19	–
30	150	–	8	29	122	33

throughout the duration of both experiments, with no indication of any dilatancy or volume increase. The total porosity reduction at failure is around 0.5% for both temperatures. At an effective pressure of 30 MPa, the stress-strain behavior of Boise sandstone (Figure 5b) is qualitatively similar to that of Bleursville sandstone in the high pressure regime, with inflexions in the stress-strain curves at 22 and 19 MPa for 20°C and 150°C, respectively. Again, the porosity change curves for both experiments at P_{eff} = 30 MPa show compaction that increases linearly with increasing axial strain throughout (Figure 5d), resulting in overall porosity reductions of around 2.2% at both temperatures.

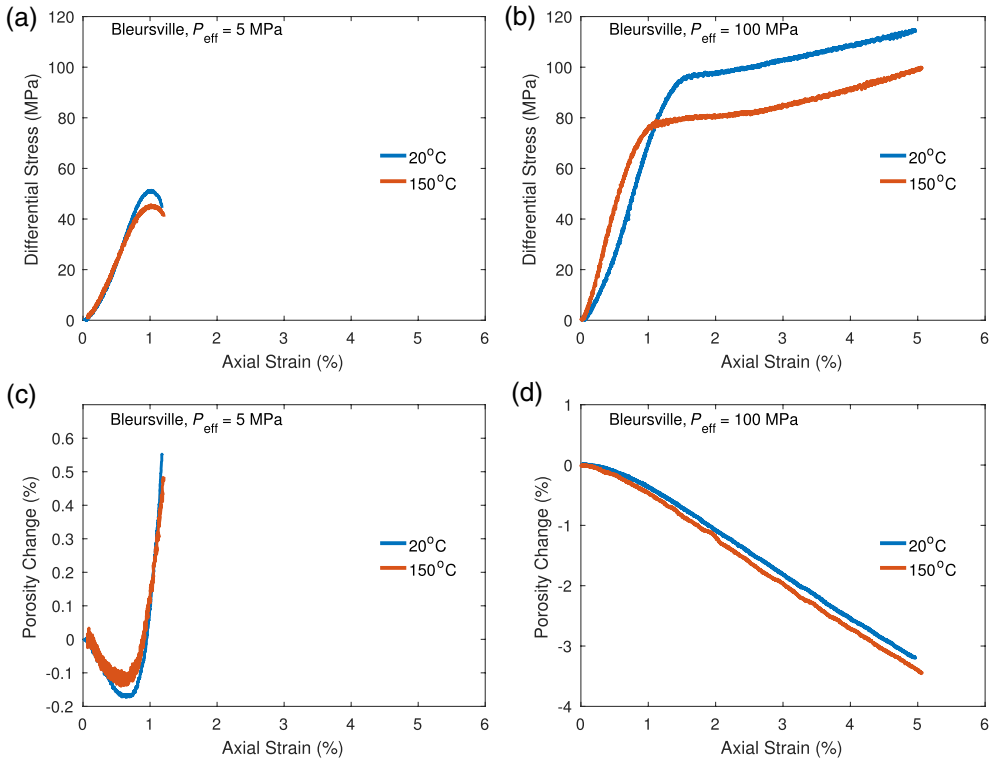

Figure 3. Differential stress and porosity change (in percentage points) as a function of axial strain for Bleursville sandstone, deformed at $P_{eff} = 5$ MPa (a),(c) and at $P_{eff} = 100$ MPa (b),(d) while at room temperature (blue curves) or 150°C (red curves).

The evolution of porosity reduction as a function of effective mean stress for all tested effective confining pressures and temperatures on Bleursville, Locharbriggs and Boise sandstone are presented in Figures 6–8, respectively. For each experiment, any deviation away from the hydrostat marks the onset of inelastic deformation, or the yield point. Deviation toward the left indicates dilatancy and porosity increase, while deviation to the right indicates compaction and porosity decrease. We term the onset point of inelastic dilatancy as C', and the onset point of inelastic compaction as C^*. For clarity, we only plot the ambient temperature hydrostat in Figures 6 and 7 since we find no significant difference between the gradient of the 20°C and 150°C curves (see Figure A1 in Appendix A).

The observed mechanical behavior was brittle, dilatant at low effective pressure ($P_{eff} = 5$ and 20 MPa in Bleursville sandstone, $P_{eff} = 5$ and 25 MPa in Locharbriggs sandstone), and was ductile, compactant at high effective pressure ($P_{eff} > 55$ MPa in Bleursville and Locharbriggs sandstone, $P_{eff} > 20$ MPa in Boise sandstone). At intermediate effective pressures (starting as low as 5 MPa in Boise sandstone), the samples exhibited strain weakening and shear failure, but experienced net compaction. In all regimes, the yield stress and either the peak stress (in the brittle/intermediate regimes) or the flow stress (in the ductile regime) were significantly lower at 150°C than at room temperature (Table 2).

For Boise sandstone, it was possible to access the hydrostatic grain crushing pressure (P^*) in our deformation apparatus at both test temperatures, and these points are indicated in Figure 8. The grain crushing pressure was reached at 38 MPa at 20°C and 35 MPa at 150°C.

By compiling all the dierent yield points (C', C^* and P^*) from all the experiments on all three sandstones in both the brittle and ductile regimes, we can construct a family of yield envelopes for each test temperature. These envelopes are presented in Figure 9, plotted in dierential stress (Q) versus eective mean stress (P) space. For Bleursville sandstone (Figure 8a), the yield points produce a near linear $Q(P)$ relation in the brittle regime, and an elliptical curve is fitted to the yield points for both temperatures in the ductile regime using the method of Wong et al. (1997) (see also Baud et al., 2000).

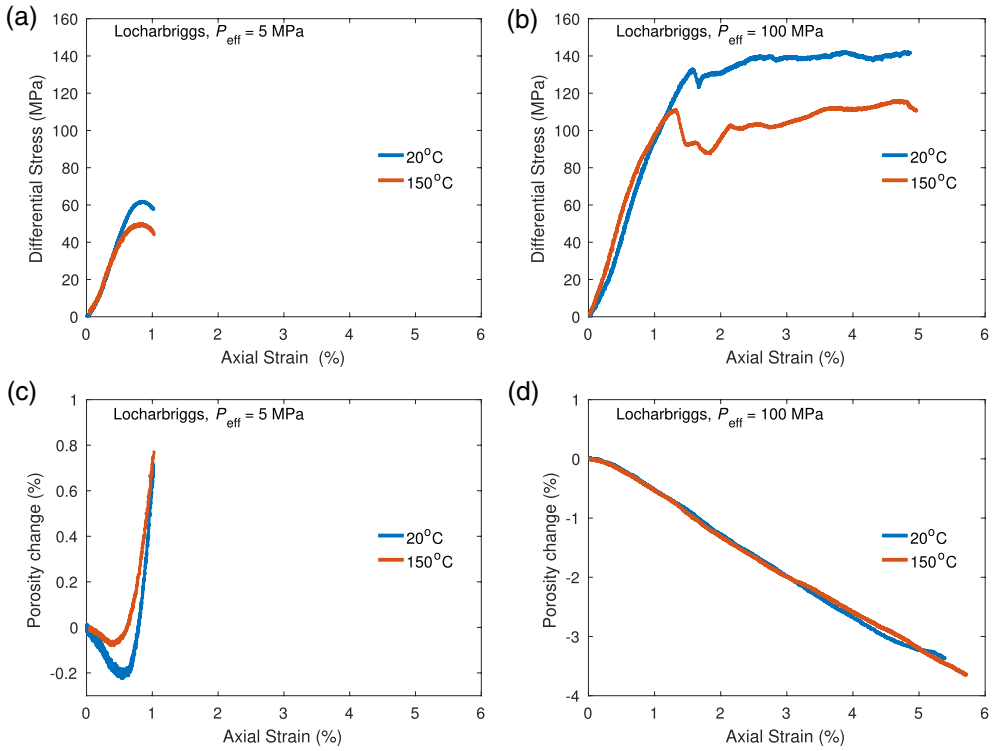

Figure 4. Differential stress and porosity change (in percentage points) as a function of axial strain for Locharbriggs sandstone, deformed at $P_{eff} = 5$ MPa (a),(c) and at $P_{eff} = 100$ MPa (b),(d) while at room temperature (blue curves) or 150°C (red curves).

The elliptical envelope is assumed to be of the form

$$P / P^* = \chi + (1 - \chi)\cos\theta, \tag{1}$$

$$Q / P^* = \delta \sin\theta, \tag{2}$$

where θ ranges from 0 to $\pi/2$ and both χ and δ correspond to dimensionless parameters with values of between 0 and 1. Wong et al. (1997) established, for a number of sandstones, that the yield envelope can be well described by Equations 1 and 2 with $\chi = 0.5$ and a value of δ between 0.5 and 0.7. Since the value of P^* was not attainable for Bleursville and Locharbriggs sandstones in our experimental setup, we used values of δ that gave the best fit to the available experimental data at each temperature. For Bleursville sandstone, this resulted in a value of $\delta = 0.51$ at 20°C, and a value of $\delta = 0.375$ at 150°C. Using these values and extrapolating the curves to $Q = 0$ gives estimated values of P^* of 160 ± 4 MPa and 150 ± 3 MPa for 20°C and 150°C, respectively. For Locharbriggs sandstone, the value of δ derived from the best fit curves was 0.50 for both temperatures, which yields values of P^* of 187 ± 5 MPa at 20°C and 162 ± 6 MPa at 150°C. Boise sandstone produced a much smaller yield envelope when compared with Bleursville and Locharbriggs sandstone (Figure 9c). We found best fit values of $\chi = 0.3$ for both temperatures and $\delta = 0.32$ and 0.28 for 20°C and 150°C, respectively.

Overall, for all three sandstones, we observe a significant contraction in the yield envelopes as temperature is raised from ambient to 150°C, indicating a concomitant reduction in the stress required to initiate inelastic deformation at elevated temperature.

6. Deformation Structures

The stress-strain curves presented earlier can, in general, be grouped into two categories. One where a sharp stress drop was observed, and one where the samples continued strain hardening until the experiment was terminated. The first category is characteristic of the brittle deformation regime and occurred at

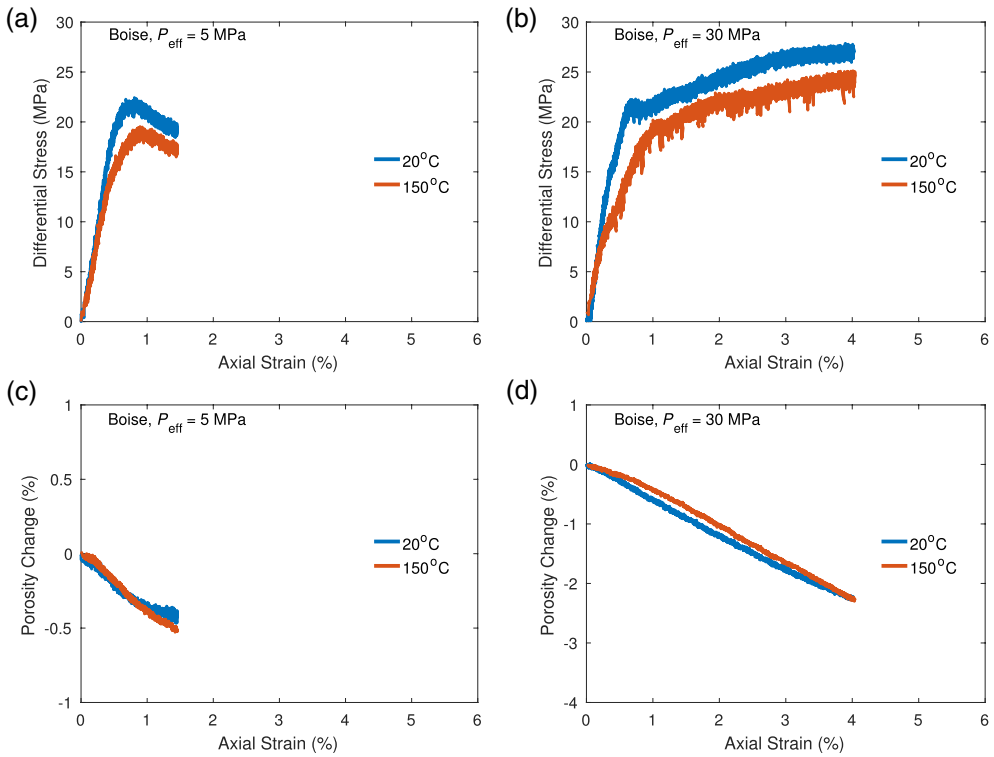

Figure 5. Differential stress and porosity change (in percentage points) as a function of axial strain for Boise sandstone, deformed at P_{eff} = 5 MPa (a),(c) and at P_{eff} = 30 MPa (b),(d) while at room temperature (blue curves) or 150°C (red curves).

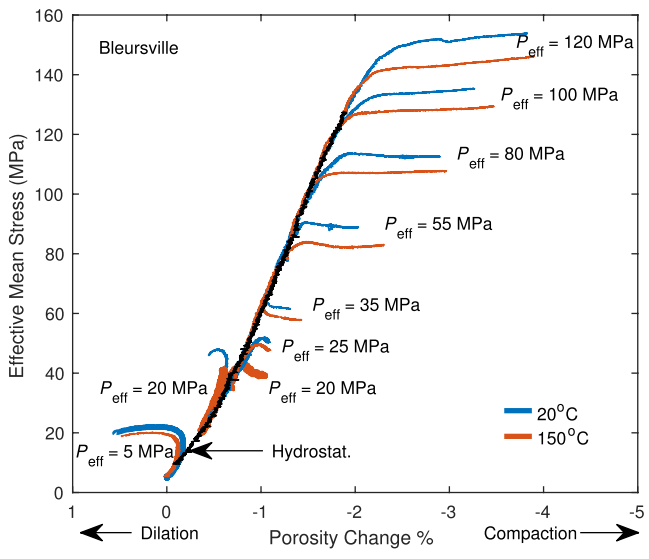

Figure 6. Porosity change (in percentage points) as a function of effective mean stress for constant strain rate experiments on Bleursville sandstone at a range of effective pressures. Blue curves indicate room temperature tests and red curves represent experiments carried out at 150°C. A deviation away from linearity marks the yield stress, with a deviation to the left indicating dilatancy and a deviation to the right indicating compaction. The black curve indicates the elastic compaction as a result of an applied hydrostatic stress.

lower effective pressures. Experiments ending in this fashion typically had a singular or a series of shear fractures running through the samples, and as shown in Figures 6–8, the samples used in these experiments underwent some degree of dilation after the yield point. The second category occurred at higher effective pressures and is therefore representative of the ductile deformation regime where compaction is occurring for the duration of the experiment. In these experiments, the samples had no clear fracture within them, and often had regions of reduced grain cohesion and increased damage. These two categories present themselves as different styles of deformation which can be seen macroscopically at the end of the experiment. Figure 10 shows two Bleursville sandstone samples deformed at an effective pressure of 5 MPa while at either room temperature or 150°C. In both samples, one sample-scale fracture can be seen running at ~30° from the direction of applied load. Most experiments which ended with a large stress drop had one large fracture running through the sample, although a few appeared to have multiple, or conjugate pairs of faults within the sample. Figure 11 shows two Bleursville sandstone samples deformed at an effective pressure of 35 MPa, while at either room temperature or 150°C. These samples are representative of Bleursville sandstone samples deformed at an effective pressure of 35 MPa and above. Both of the samples exhibit areas where the material is less cohesive than the macroscopically undamaged areas of the rock. The sample deformed at a temperature of 150°C has a horizontal crack running through the sample, which was most probably formed during the extraction of the sample from the pressure vessel

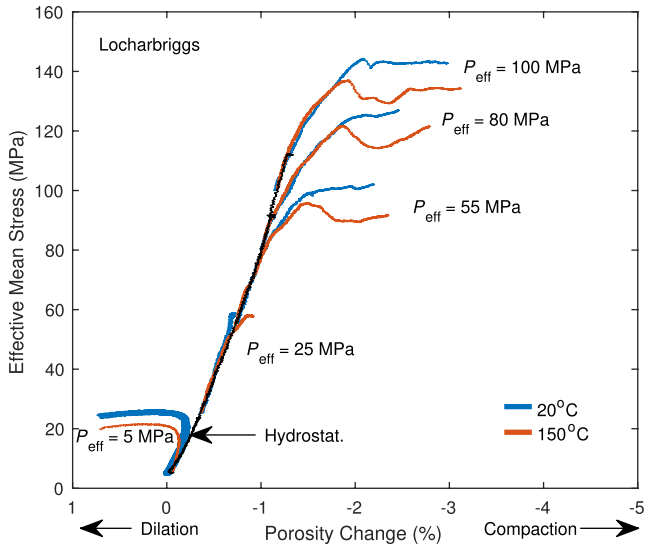

Figure 7. Porosity change (in percentage points) as a function of effective mean stress for constant strain rate experiments on Locharbriggs sandstone at a range of effective pressures. Blue curves indicate room temperature tests and red curves represent experiments carried out at 150°C. A deviation away from linearity marks the yield stress, with a deviation to the left indicating dilatancy and a deviation to the right indicating compaction. The black curve dicates the inelastic compaction as a result of an applied hydrostatic stress.

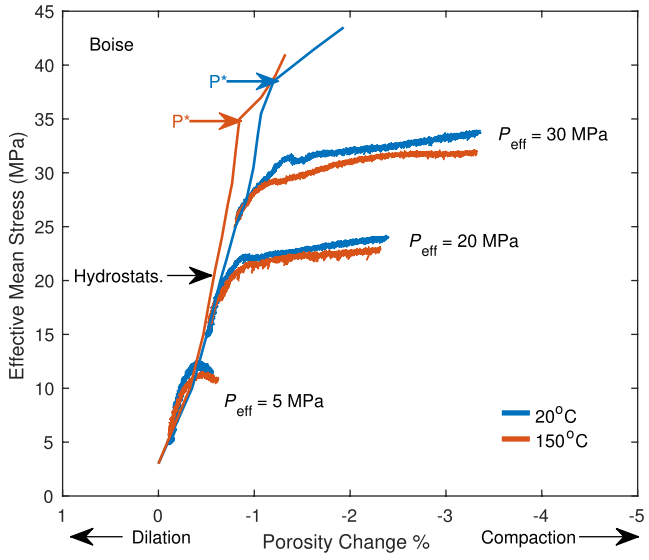

Figure 8. Porosity change (in percentage points) as a function of effective mean stress for constant strain rate experiments on Locharbriggs sandstone at a range of effective pressures. Blue curves indicate room temperature tests and red curves represent experiments carried out at 150°C. A deviation away from linearity marks the yield stress, with a deviation to the left indicating dilatancy and a deviation to the right indicating compaction. The curves labeled hydrostats, indicates the compaction as a result of an applied hydrostatic stress, with the deviation away from linearity indicating the *P*value*.

or jacket. To the eye, there appears to be no macroscopically difference between the samples deformed at room temperature and at elevated temperature.

Figures 10 and 11 include BSE micrographs of each of the samples represented in the macroscopic photos. The location of the selected micrographs is indicated on a BSE scan of the whole sample. These locations were chosen as they represent areas of the sample which have experienced the greatest amount of deformation. For the samples deformed at an effective pressure of 5 MPa, the regions of high damage are located close to the sample scale fracture. In the samples deformed at an effective pressure of 35 MPa the highly damaged regions are much broader than the samples deformed at lower pressure, and correspond to the areas of reduced cohesion in the macroscopic photos. BSE micrographs of the regions of the samples which are relatively undamaged are presented in Appendix B, Figures B2, and B3.

At an effective pressure of 5 MPa the area surrounding the shear fracture includes highly fractured grains which due to the massively reduced grain size exhibit signs of cataclasis. Slightly further away from the large shear fracture, the grains exhibit intragranular (within a single grain), intergranular (along grain boundaries), and transgranular (across multiple grains) fracturing. All of these deformation features are visible in the sample deformed at room temperature and at 150°C, which indicates that similar mechanical processes are driving the deformation at both temperatures. For the samples deformed at an effective pressure of 35 MPa, the sample scale scan indicates that both samples contain small sub-horizontal cracks running the breadth of the sample. Due to the orientation of these fractures, the most likely explanation is they formed during the extraction of the sample from the vessel or jacket. The location of these cracks are also indicative of the highly damaged regions within the sample. The BSE micrographs show that many of the grains are highly fractured and the preferred orientation of these fractures is vertical to sub-vertical. The fractures often originate from contacts with other grains, which is a indicative of Hertzian style fracturing. In comparison to the relatively undamaged regions, shown in Appendix B, Figures B2 and B3, it is observed that there is a drastic reduction in the visible porosity, which results from infilling of the pore space by crushed grains. There does appear to be a slightly higher crack density in the sample deformed at room temperature compared to the sample deformed at 150°C. The most probable explanation for this, is that at room temperature the sample was taken to 5.5% axial strain compared to 4.1% strain for the sample deformed at 150°C. Regrettably, sample preservation in this study was poor and a full in-depth microstructural analysis which would offer a more statistically meaningful insight was not possible. Despite the slight difference in apparent crack densities, it would appear that the same physical processes are occurring at both temperatures. In the samples deformed at 150°C, we did not detect any evidence of additional pressure solution features beyond those already present in the undeformed rock.

Figure 12 shows a micrograph of the hydrostatically deformed Boise sandstone sample at room temperature presented in Figure 8. In this image, many of the grains have been fractured, indicating that inelastic deformation has occurred at a stress 5 MPa past *P**, this is in contrast to

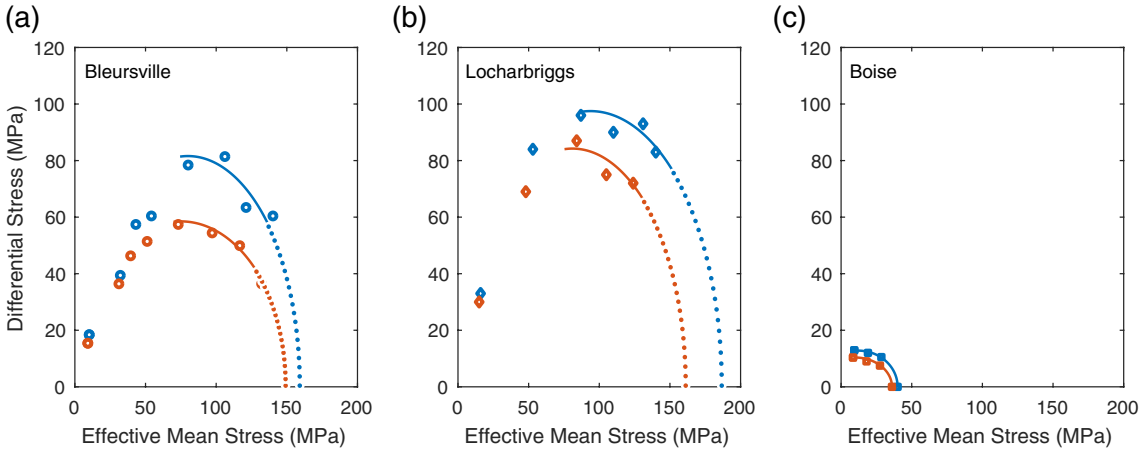

Figure 9. The yield stresses picked for all experiments displayed in effective mean stress versus differential stress space for (a) Bleursville sandstone, (b) Locharbriggs sandstone, and (c) Boise sandstone. Blue symbols are for room temperature tests and red symbols for 150°C tests. An ellipse is fitted to the data in the ductile regime, with the dotted part corresponding to the areas of extrapolation.

the undeformed sample presented in Figure 1. The fractures do not indicate any preferred orientation and seem randomly distributed throughout the sample.

7. Discussion

7.1. Mechanical Behavior

The differential stress versus axial strain curves shown in Figures 3–5 at 5 MPa effective confining pressure are characteristic of sandstone deformation in the brittle regime (Baud et al., 2000; Wong et al., 1997). The initial concave up phase is typically associated with the closure of pre-existing microcracks and pores, and is followed by a quasi-linear elastic phase up to C'. When C' is reached, dilatant microcracking initiates within the sample and the net amount of compaction is reduced, causing the deviation away from linearity of the porosity evolution curves in Figures 3 and 4. With increasing stress, dilatant microcracking becomes dominant and the net change in sample volume becomes positive and dilatant. Increasing the temperature to 150°C did not alter the general shape of the curves for all three sandstones. However, the values of C' and peak stress are reduced by 9%–17% in Bleursville sandstone, and by 10%–19% in Locharbriggs sandstone. This is comparable to results reported by Heap, Baud, Meredith (2009) where an increase in temperature from room temperature to 75°C corresponded to a reduction in C' by 6%–10 % for Bentheim, Darley Dale, and Crab Orchard sandstones. In Boise sandstone (Figures 5a and 5c), compaction is dominant throughout the experiments at $P_{\text{eff}} = 5$ MPa and all temperature tested, which indicates that the samples accommodated deformation by localized compaction within compactant shear bands.

At intermediate effective pressure (Bleursville sandstone at $P_{\text{eff}} = 20$ MPa and Locharbriggs sandstone at $P_{\text{eff}} = 25$ MPa), the behavior is transitional between dilatant-brittle and purely compactant-ductile. Under those conditions, more compaction is observed in the samples tested at 150°C than at room temperature (Figures 6 and 7), which implies that higher temperatures would tend to lower the stress conditions for the brittle-ductile transition.

At elevated effective pressure ($P_{\text{eff}} > 50$ MPa in Bleursville and Locharbriggs sandstone, $P_{\text{eff}} > 20$ MPa in Boise sandstone), the mechanical behavior is characteristic of the ductile regime: the yield point is marked by increased compaction, which is the result of intragranular cracking and grain crushing. This behavior is qualitatively similar at 150°C and at room temperature, but with a systematic reduction in yield stress and flow stress (by 6%–37% depending on the rock) at higher temperature.

The weakening effect due to the temperature increase is in general more pronounced in the ductile regime than the brittle regime when measured in terms of the absolute stress reduction (Figure 9). In the following,

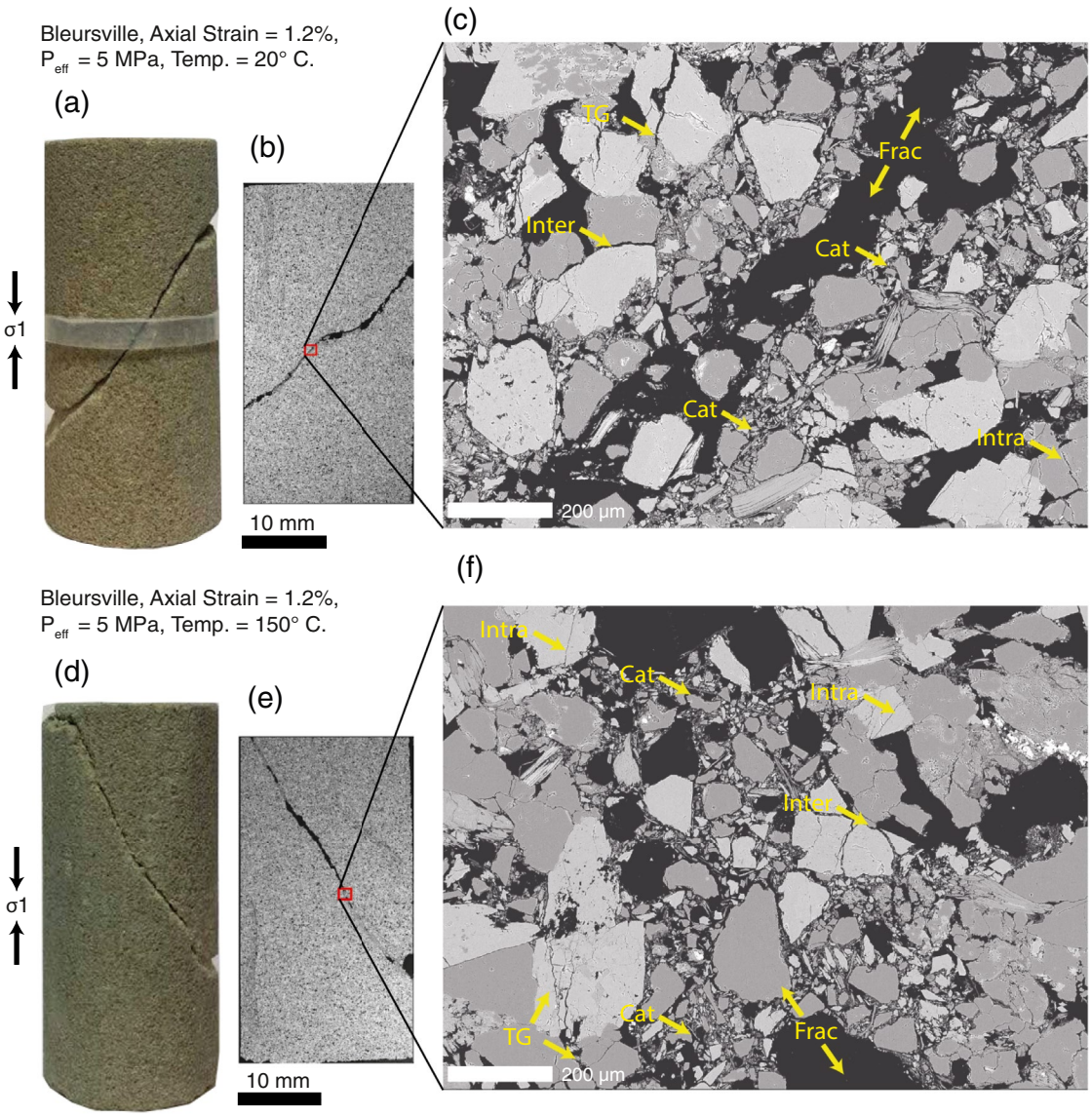

Figure 10. Bleursville sandstone samples deformed at P_{eff} = 5 MPa, and either room temperature (a, b, and c) or 150°C (d, e and f) to ~1.2% axial strain before failure. In all images, the compressional axis is vertical. Included is a photo of the sample post deformation (a) and (d), a BSE scan of ~40 mm of the 53 mm long sample (b) and (e), and a 100 times zoom of a highly damaged area (c) and (f), the location of which is indicated by the red box on parts b and (e) The photos and the sample scale BSE scans have the same scales which are indicated by the 10 mm scale bars. Additionally, they are only aligned in the direction of compression and not necessarily on the viewing axis. In parts c and f, the yellow notations are: Inter, intergranular (grain boundary) fracturing; Intra, intragranular (within singular grain) fracturing; TG, transgranular (across multiple grains) fracturing; Frac, sample scale fracture; Cat, cataclastic texture.

we examine the possible mechanisms that can explain the weakening produced by relatively modest temperature increase (here only 130°C) under water saturated conditions.

7.2. Mechanism of Temperature Weakening

Three primary mechanisms can be considered to explain the weakening observed at elevated temperature: intergranular pressure solution, a reduction in fracture toughness or an increase in crack growth kinetics. From the limited microstructural observations, we have inferred that there is no observable difference in the micromechanical process occurring at either room temperature or at 150°C, and elevated temperature appears to only impact the stress level at which deformation occurs.

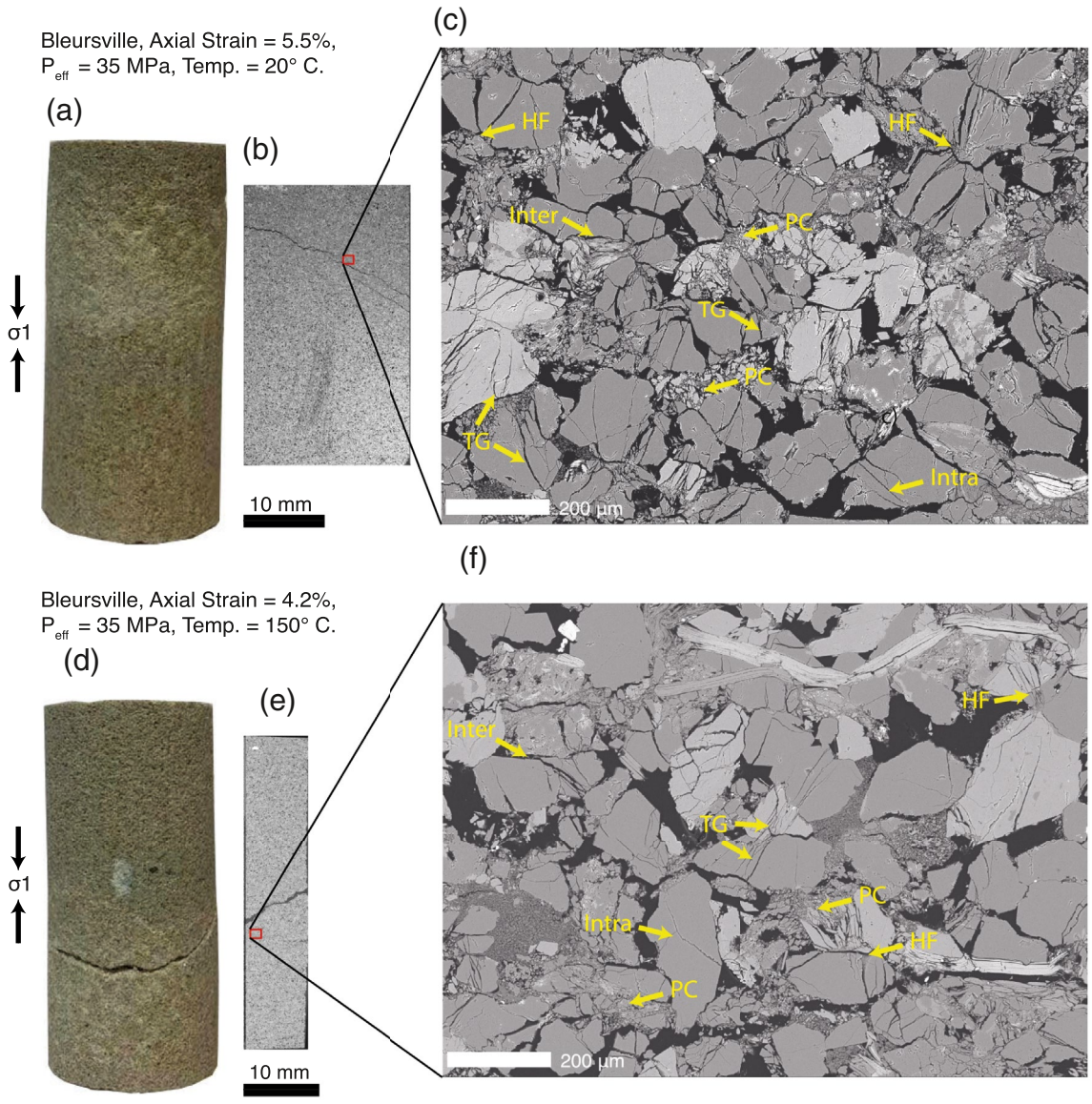

Figure 11. Bleursville sandstone samples deformed at P_{eff} = 35 MPa, and either room temperature (a, b, and c) or 150°C (d, e and f) to 5.5% (a, b and c) or 4.2% (d, e and f) axial strain. In all images the compressional axis is vertical. Included is a photo of the sample post deformation (a) and (d), a BSE scan of ~40 mm of the 53 mm long sample (b) and (e), and a 100 times zoom of a highly damaged area (c) and (f), the location of which is indicated by the red box on parts b and (e) The full BSE scan in part e, is only half the width of the other sample scans displayed in the manuscript. The photos and the sample scale BSE scans have the same scales which are indicated by the 10 mm scale bars. Additionally, they are only aligned in the direction of compression and not necessarily on the viewing axis. In parts c and f, the yellow notations are: Inter, intergranular (grain boundary) fracturing; Intra, intragranular (within singular grain) fracturing; TG, transgranular (across multiple grains) fracturing; PC, pore collapse and grain crushing; HF, Hertzian style fracturing.

7.2.1. Intergranular Pressure Solution

Intergranular pressure solution involves the dissolution of grain material at highly stressed grain contacts prior to the diffusion and precipitation of this material to lower stressed grain boundaries. This process is known to have a temperature dependence and 150°C is often seen as the lower bound temperature at which it is detectable in quartz rich rocks (e.g., Niemeijer et al., 2002; Rutter, 1976). Using a dissolution limited pressure solution model combined with theoretical values utilized in previous studies (Niemeijer et al., 2002; X. Zhang et al., 2010), it is possible to calculate the expected strain rate due to pressure solution at 150°C. This model assumes dissolution is the limiting factor in the rate of pressure solution and uses an

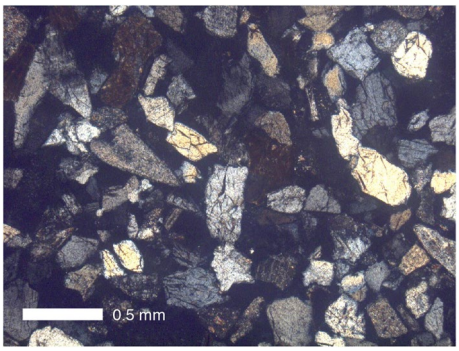

Figure 12. An optical micrograph in crossed polarized light of Boise sandstone hydrostatically deformed to 43 MPa, which is 5 MPa higher than the inferred value of P^*.

assemblage of spherical quartz grains packed in a simple cubic arrangement so that the strain rate due to pressure solution is

$$\dot{\epsilon} = 6\Omega \times 10^{(1.174-0.002028T-4158/T)}\left[\exp\left(\frac{BP\Omega}{RT}\right)-1\right]\frac{f}{d}, \quad (3)$$

where $\dot{\epsilon}$ is the volumetric strain rate, Ω is the molar volume of quartz, T is the temperature, d is the grain diameter, f a non-dimensional grain packing factor, B a stress amplification factor, R is the Boltzmann constant, and P the effective pressure. Both the grain packing factor and the stress amplification factor are a function of the matrix geometry and for simple, regular geometries can be calculated explicitly. However, due to the more complex and irregular arrangement of grains in natural samples, these calculations become much more convoluted and are not necessary for order of magnitude computations. Therefore following X. Zhang et al. (2010), we deem it appropriate to assume a value of one for the stress amplification factor and a value of six for the grain packing factor.

When a grain diameter of 0.1 mm is used at an effective pressure of 100 MPa, the theoretical strain rate would be of the order of 10^{-9} s^{-1} at 150°C. As this is four orders of magnitude lower than the imposed axial strain rate, it would suggest that pressure solution would not play a significant role in sandstone compaction under our laboratory conditions. This is in agreement with Figures 10 and 11 which show that microcracking is heavily present in the samples deformed at 150°C, while no significant evidence of pressure solution features (beyond those already present in the intact rock) could be detected.

7.2.2. Reduction in Internal Friction and Fracture Toughness

The weakening observed at elevated temperature is analogous to the water weakening effect analyzed by Baud et al. (2000), which was interpreted as a reduction in surface energy. Here, we adopt a similar approach and propose that a reduction in fracture toughness at elevated temperature can explain the observed weakening.

Many previous studies have identified that the inelastic compaction of porous rocks is accommodated by grain crushing and the infilling of pore space (Menéndez et al., 1996; Wong & Baud, 2012; J. Zhang et al., 1990). Grain crushing is initiated by the propagation of Hertzian cracks due to the high compressive stresses generated at the small contact area between two adjacent grains. This microfracturing process can only occur at high confining pressure, since high normal stresses are needed to prevent any slip between grains or along pre-existing microcracks. Wong et al. (1997) showed that the elliptical yield envelope for porous sandstone scales with the magnitude of P^*. It would therefore follow that the shrinkage of the compactive yield envelope due to the temperature increase should correspond to a reduction in the magnitude of P^*; this is indeed the case in Boise sandstone (for which P^* could be reached in our apparatus; see Figure 8).

Under purely hydrostatic conditions, J. Zhang et al. (1990) showed that the grain crushing pressure P^* in granular aggregates is given by

$$P^* = 2.2\frac{(1-\nu^2)^2}{E^2(1-2\nu)^3}\frac{K_{IC}^3}{(\phi c)^{3/2}}, \quad (4)$$

where ν and E are the Poisson's ratio and Young's modulus of the grains, ϕ is the porosity of the aggregate, K_{IC} is the critical value of the stress intensity factor and c the length of pre-existing microcracks at the grains surface.

The data presented in Figure A1 showed that under hydrostatic loading the increased temperature increased the elastic compaction of Bleursville sandstone by ~15%. Taking the gradients of the elastic portion of the stress-strain curves shown in Figures 3–5, it is possible to compute the Young's modulus of each sample. The average calculated Young's moduli were 9.3 GPa and 8.3 GPa for Bleursville sandstone at room temperature and 150°C respectively. For Locharbriggs sandstone, the Young's modulus was

10.2 GPa and room temperature and 11.2 GPa at 150°C, and for Boise sandstones the values were 4.0 GPa at room temperature and 2.8 GPa at 150°C. Figure A2 shows the Young's modulus as a function of effective pressure for each rock type, and it can be seen for Bleursville and Locharbriggs in particular, that there is no clear correlation between the Young's modulus and either the effective pressure nor the temperature. For Boise sandstone the Young's modulus is consistently lower at 150°C than room temperature for all experiments. However, the reduction observed in Boise sandstone at elevated temperature is on the order of 1 GPa, which is much lower than the ± 4 GPa deviation from the average that all three rocks exhibited. Combined with the hydrostatic deformation curves, it is therefore probable that the elastic modulus of the rocks is only being altered by negligible amounts as a result of the increased temperature. If we further consider that the pre-existing crack length and porosity are also unchanged by moderate changes in temperature, any decrease in P^* at elevated temperature can be represented in a reduction in the magnitude of K_{IC} to a lower value. The ratio between the room temperature value of P^* and the value at 150°C is thus

$$\frac{P^*_{150}}{P^*_{20}} = \left(\frac{K_{IC(150)}}{K_{IC(20)}} \right)^3, \tag{5}$$

where subscripts denote the temperature in °C.

The P^* values measured in the experiments or estimated from the extrapolated yield curves (Table 3) show that a reduction of just 3%–4% in K_{IC} is sufficient to explain the observed reduction in yield stress in the compactant regime.

In addition to a reduction in yield stress in the ductile, compactant regime, our results also show that the temperature increase also tends to reduce the yield stress in the brittle, dilatant regime, but in smaller proportions. This can be understood by considering a simple conceptual fracture mechanics model for yield in the brittle regime. Several approaches have been proposed to model the yield stress in the brittle regime, which is generally attributed to the onset of mode I crack opening around preexisting flaws such as grain boundaries, sliding cracks or pores (e.g.,Ashby and Hallam, 1986; Ashby & Sammis, 1990; Nemat-Nasser & Horii, 1982; Sammis & Ashby, 1986). Here we follow the choice of Baud et al. (2000) and use the sliding wing crack model, which, in its simplest form, considers isolated, two dimensional preexisting closed microcracks (e.g., a grain boundary) that can slide with a static friction coefficient μ. With increasing axial stress σ_1 at a given lateral stress σ_3, the preexisting microcracks will start sliding once the frictional forces are overcome. The sliding motion imparts a tensile stress at the crack tips, which eventually leads to the nucleation and growth of tensile "wings" emanating from the original sliding flaw. The stress state at the onset of tensile fracturing at the tips of microcracks optimally oriented for sliding is given by Ashby and Hallam (1986)

$$\sigma_1 = \frac{\sqrt{1+\mu^2}+\mu}{\sqrt{1+\mu^2}-\mu}\sigma_3 + \frac{\sqrt{3}}{\sqrt{1+\mu^2}-\mu}\frac{K_{IC}}{\sqrt{\pi a}}, \tag{6}$$

where a is the half-length of the sliding crack. At a given friction coefficient and confining pressure, the yield stress in the brittle regime scales linearly with $K_{IC} / \sqrt{\pi a}$, whereas the grain crushing pressure P^* and thus the yield stress in the ductile regime scales with $(K_{IC} / \sqrt{\pi c})^3$ (see Equation 4). This is qualitatively consistent with our observation that an increase in temperature, if indeed responsible for a reduction in fracture toughness, would have a stronger weakening effect in the ductile regime compared to the brittle regime. Such considerations are somewhat independent from the specific choice of model for the brittle yield stress, since most models based on fracture mechanics, including those involving crack growth from open pores (Sammis & Ashby, 1986; Wong, 1990), generally predict that the critical stress at yield point in the brittle regime scales linearly with $K_{IC} / \sqrt{\pi a}$, where a is the dimension of the defect from which tensile cracks emanate.

Despite this general qualitative agreement, quantitative consistency is difficult to establish. In Bleursville sandstone, at an effective pressure of 5 MPa the onset of dilatancy occurred at 18 MPa differential stress. If a friction coefficient of 0.6 is used, which is common to most rocks (Byerlee, 1978), we infer from Equation 6

Table 3
The Inferred and Measured Values of P, the Ratio of P* at Room Temperature and 150°C, and the Percentage Reduction in the Value of P* and K_{IC} at Elevated Temperature*

Rock type	P^*_{20} MPa	P^*_{150} MPa	$\frac{P^*_{150}}{P^*_{20}}$	K_{IC} reduction
Bleursville	160	150	0.94	3%
Locharbriggs	188	162	0.86	4%
Boise	40	36	0.9	3%

that $\frac{K_{IC}}{\sqrt{\pi a}}$ is approximately equal to 2.5 MPa, which is of similar magnitude to values found by Wu et al. (2000) for Darley Dale (3.21 MPa) and Berea sandstones (4.71 MPa). From our analysis in the ductile regime (Equation 5), we have inferred a 3% reduction in the value of K_{IC} at 150°C, which would correspond to only a 0.2 MPa or approximately 1% reduction in the differential stress at C'. This small, almost negligible reduction in yield stress is inconsistent with our data, which indicate that a temperature increase to 150°C reduced the onset of dilatancy by 8%–18% (Table 2). To achieve a reduction in yield stress at C' of up to 18%, K_{IC} would need to decrease by nearly 40%, which cannot be reconciled with the data in the ductile regime.

One way to solve the quantitative discrepancy between the inferred reduction in K_{IC} from the ductile regime and the data in the brittle regime is to assume that an increase in temperature also leads to a decrease in internal friction coefficient. If the coefficient of friction is reduced from 0.6 to 0.55 in combination with a 4% reduction in K_{IC}, the reduction in differential stress at C' in Bleursville sandstone at 5 MPa effective confining pressure is of around 3 MPa, i.e., 17%, which is in agreement with our data. Such a small decrease in friction at 150°C is of similar magnitude to that inferred by Baud et al. (2000) from dry to water-saturated conditions.

Overall, our analysis based on micromechanical models shows that a modest reduction in fracture toughness, by a few percent, is sufficient to explain the observed shrinkage of the yield envelope at 150°C. An additional small reduction in internal friction, by around 10%, appears to be necessary to quantitatively explain the decrease in yield stress in the brittle, dilatant regime. The inferred decrease in fracture toughness with increasing temperature is consistent with the decrease of fracture energy in quartz single crystals reported by Darot et al. (1985). It is also broadly consistent with fracture toughness measurements obtained on bulk rock samples for mode I cracks much larger than the grain size; although an initial slight increase in toughness is typically measured from room temperature to around 100°C in most rocks (e.g., Balme et al., 2004; Feng et al., 2018; Meredith & Atkinson, 1985), the increase is generally attributed to microcrack toughening that leads to local arrest of the macroscopic fracture (Lawn, 1993). Such structural effects are not expected to be operative at the scale of microcracks propagating at the grain scale, which explains why our results are more consistent with single crystal rather than bulk rock toughness measurements.

The inferred decrease in internal friction is more challenging to relate to independent measurements. While a wealth of rock deformation literature has been devoted to measuring friction coefficient in rocks and gouges, the effect of temperature up to 150°C is very subtle (e.g., Blanpied et al., 1995). Qualitatively, experiments conducted on quartz gouge tend to show that increasing temperature produces a weakening (Chester, 1994), which is consistent with our data. However, Chester (1994) interpreted this weakening as a bulk phenomenon in gouge resulting from thermally activated crack growth kinetics, and it is not clear that this effect should occur at the microscopic scale relevant to the wing crack model, which clearly separates friction and cracking processes. In pure quartz sand, Karner et al. (2008) report a negligible effect of temperature on the yield behavior at low effective confining pressure. Our results would therefore imply that feldspar and clays play a role in the observed weakening at increasing temperature. In this respect, the effect of temperature is very similar to the effect of water on the yield envelope of sandstones, which is negligible in pure quartz sandstones (Reviron et al., 2009) but is significant in feldspar- and clay-bearing sandstones (Baud et al., 2000).

7.2.3. Increase in Crack Growth Kinetics

In the previous Section we interpreted the weakening of sandstone due to a moderate temperature increase as due to a small reduction in fracture toughness. Fracture toughness can be considered as an upper bound for the stress intensity factor required to propagate a microcrack: at stress levels such that $K_I < K_{IC}$ and in chemically active environments (such as water), cracks tend to propagate subcritically due to chemical reactions occurring at highly stressed fracture tip (e.g., Anderson & Grew, 1977; Atkinson, 1984; Lawn, 1993). Subcritical crack growth is generally considered to result from thermally activated processes, and in silicate

rocks and quartz single crystals even a relatively modest increase in temperature, of the order of a few tens of degrees, can produce orders of magnitude increases in crack growth rate (e.g., Darot & Guéguen, 1986; Meredith &, Atkinson, 1985). Here, we examine the possibility that the apparent decrease in fracture toughness at elevated temperature could be the manifestation of the temperature dependence of subcritical cracking.

In order to establish how changes in crack growth kinetics can be connected to changes in strength, we first need to recall the key end-member cases in the possible relationships between applied stresses and crack growth rate. Based on the framework of irreversible thermodynamics, Rice (1978) derived a general relationship between crack growth rate v, the energy release rate G, and surface energy γ:

$$(G - 2\gamma)v > 0, \tag{7}$$

where we recall that G is related to the stress intensity factor K_I as

$$G = \frac{1 - \nu^2}{E} K_I^2. \tag{8}$$

Equation 7 implies that G is expected to be larger than twice the surface energy for crack growth to occur at any appreciable rate. In general, subcritical crack growth rate is observed to vary as a function of G according to one of three main regimes (schematically shown in Figure 13): for G near 2γ (regime I), crack growth rate is limited by reaction rate at the crack tip; at increasing G (regime II), crack growth rate is limited by the diffusion rate of chemical species to the crack tip; at large G (regime III), crack growth becomes rate independent and is controlled by the strength of atomic bonds within the material. It is generally considered that the fracture energy $G_c = (1 - \nu^2)K_{IC}^2 / E$ corresponds to the upper bound of G for "fast" crack propagation (where v can be as high as the Rayleigh wave speed of the material), so that $G_c - 2\gamma > 0$ includes dissipative processes (Guéguen & Palciauskas, 1994; Maugis, 1985). For $2\gamma < G < G_c$, crack growth rate is expected to be nonzero and is influenced by environmental conditions, notably chemical activity of species in contact with the crack surface, as well as temperature (Rice, 1978).

Our experiments were all conducted at constant strain rate. One possibility is that crack growth rate is always high, so that deformation is primarily driven by increasing stress and crack propagation is well described by a simple $G = G_c$ criterion. In that scenario, rate effects are negligible, and the weakening observed at high temperature would be the direct consequence of a decrease in K_{IC}, i.e., a decrease in G_c to G'_c. However, the underlying physical process driving the decrease in toughness with increasing temperature is unclear: Darot et al. (1985) report a decrease in fracture energy in quartz at elevated temperature, which was interpreted as a decrease in surface energy γ. In principle, a decrease in γ could lead to a decrease in G_c (Figure 13, red dashed curve), but this would require that the dissipation processes involved in G_c remain comparable to 2γ. An alternative analysis is that, with increasing temperature, rate effects such as subcritical crack growth become significant and allow crack growth to occur at $G < G_c$.

It is in general difficult to relate explicitly the macroscopic strain rate to microscopic crack growth rates: any such relation strongly depends on detailed assumptions about the microcrack geometry, and realistic models tend to be intractable. However, some progress can be made if we assume that crack growth is the limiting step to accumulate strain; this is the case for instance in time-dependent wing crack models that assume constant friction on the sliding flaw (e.g., Brantut et al., 2012, 2014). In that framework, the instantaneous strain rate is, to first order, proportional to the microcrack growth rate. In the regime where crack growth is limited by reaction rate, which seems to be the dominant one observed in most fracture growth tests in rock forming minerals (Atkinson, 1984), subcritical crack growth rate can be derived from the theory of thermally activated process, which yields an expression of the following form: (e.g., Darot & Guéguen, 1986; Wan et al., 1990)

$$v = v_0 \exp\left(\frac{-E^*}{kT}\right) \sinh\left(\frac{b\ell(G - 2\gamma)}{2kT}\right), \tag{9}$$

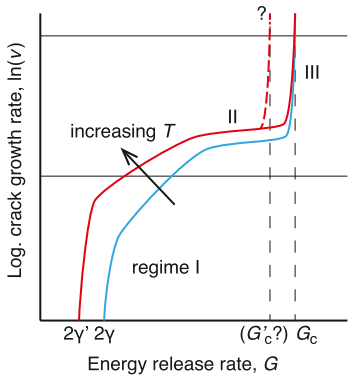

Figure 13. Schematic of subcritical crack growth rate as a function of energy release rate. The dashed part of the curve illustrates a potential decrease in G_c down to a lower value G_c' at elevated temperature, which would produce a weakening in the rate-insensitive scenario. If subcritical crack growth is active (rate-sensitive case), an increase in temperature at a given crack growth rate would lead to a decrease in G, effectively reducing the strength of the rock.

where v_0 is a reference, constant crack velocity, E^* is an activation energy, k is Boltzman's constant, T is the absolute temperature, ℓ is the crack front length and b is an elementary step size associated with the subcritical cracking process. For G significantly greater than 2γ, the hyperbolic sine can be well approximated by a simple exponential function. Equation 9 implies that increasing temperature may have a threefold effect: (1) it directly amplifies crack growth rate by a factor given by the exponential term, (2) it reduces the sensitivity of crack growth rate to energy release rate, and (3) potentially accelerate crack growth if γ is reduced. These effects are depicted schematically in Figure 13. Maintaining a given crack growth rate v to reflect the imposed constant strain rate in our experiments, and further assuming for simplicity that γ is constant, the relative change in energy release rate ΔG associated with a change in temperature ΔT is

$$\frac{\Delta G}{G} = -\frac{\Delta T}{T}\left[\frac{2E^*}{b\ell G} - \left(1 - \frac{2\gamma}{G}\right)\right]. \tag{10}$$

The relative decrease $\Delta G/G$ depends on G itself, which for quartz ranges from a lower bound $2\gamma \approx 1$ J/m^2 (Parks, 1984) up to around 12 J/m^2, as reported from fracture toughness measurements (e.g., Atkinson, 1979). Using kinetic parameter values determined for quartz in water by Darot & Guéguen (1986), $E^* = 2.5 \times 10^{-19}$ J/molecule, $b\ell = 1.8 \times^{-20}$ m^2, we find that $\Delta G/G$ ranges from −11.7 to − 0.59 for a temperature rise from 25°C to 150°C. A reduction of G by around 60% corresponds to a reduction in K_I by around 35%, which is an order of magnitude greater than the upper range of our observations. It is therefore unlikely that the weakening effect of temperature is due to an increase in subcritical crack growth rates, reducing the energy release rate (or, equivalently, the stress intensity factor) required for crack growth at a given rate.

We attempted to further test this hypothesis by conducting two additional experiments on Bleursville sandstone at room temperature and 150°C, an effective pressure of 100 MPa, and at a higher strain rate of 10^{-4} s^{-1}. Figure 14 shows the stress strain curves for these additional experiments in comparison to the experiments performed at 10^{-5} s^{-1}. At a given temperature, there is no discernible difference in mechanical behavior between the two strain rates. This is in agreement with the hypothesis that subcritical crack growth does not control the strength at the tested strain rate. Indeed, Equation 9 implies that a change in crack growth rate from v to v' is associated to a change in energy release rate from G to G' expressed as

$$G' - G = \frac{2kT}{b\ell}\ln(v' / v). \tag{11}$$

Using the parameter values obtained for wet quartz and a ten-fold increase in v, we obtain an increase in G of the order of 1.5 J/m^2. This is at least a 10% increase in G, which should be observable in the stress-strain curves. Therefore, we conclude that subcritical crack growth in regimes I and II is not likely to be the dominant process controlling the strength of sandstones at the tested strain rates. This conclusion is drawn from a simple assumption that crack growth rate reflects the macroscopic strain rate, and using parameter values relevant to quartz only.

Even though kinetic effects may not be dominant in the range of strain rate and temperature investigated here, some evidence of time-dependent phenomena can be inferred in our data on Boise sandstone, for which P^* could be directly measured. As mentioned previously, Wong et al. (1997) have shown the elliptical yield cap scales with the value of P^*, and if this holds true for Boise sandstone the normalized yield envelopes at both room temperature and 150°C should collapse on to one another. This is not exactly the case (Figure 15): the normalized yield envelope at 150°C is slightly smaller than at room temperature. The different experimental methods used to determine the yield stress in hydrostatic (P^*)

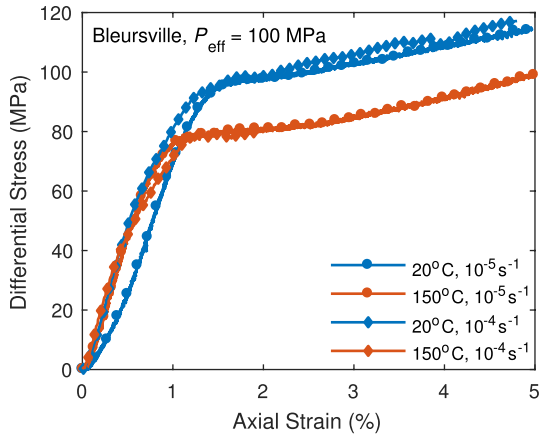

Figure 14. Differential stress against axial strain for Bleursville sandstone deformed at an effective pressure of 100 MPa at room temperature (blue) or 150°C (red) at either 10^{-4} s^{-1} (diamonds) or 10^{-5} s^{-1} (circles).

and triaxial conditions (C^*) could be a cause of this small difference. The P^* stress value is obtained by increasing hydrostatic pressure in steps, with each step occurring after the pore volume of the sample has stopped both elastically compacting and creeping at a volumetric strain rate of 10^{-8} s^{-1} or less. This means that prior to each pressure step, the majority of microcracks are in equilibrium with the chemical environment, and any crack growth rates are below detectable laboratory levels. By ensuring that the pressure steps are small, it only take minimal amounts of subcritical crack growth for the cracks to return to equilibrium with the environment. Therefore, the sudden increase in porosity reduction at P^* should be mainly a manifestation of K_I reaching K_{IC} (i.e., in the context of Figure 13, a sudden, dramatic acceleration in crack growth rate). This is in contrast to the constant strain rate tests, where the gradual, continuous increase in stress implies that the crack population is never in equilibrium with the environment and so is experiencing the deformation effects of both K_I approaching K_{IC} and subcritical cracking. It therefore follows that the slightly larger reduction in the stress at C^* than P^* with increasing temperature could then be explained by a greater contribution of chemically driven subcritical cracking during the constant strain rate tests.

Another potential mechanism which could be considered to contribute to weakening observed at 150°C include thermal induced microcracking and the dehydroxylation of clays. Extensive thermal microcracking caused by the expansion of constituent minerals has been observed in thermally treated unconfined sandstone samples above 200°C, and below 200°C thermally induced microcracking has been measured to be minimal. Using SEM imagery Jian-ping et al. (2010) concluded that for a sandstone of similar composition but much lower porosity, the first microcracks were detected at 140°C while at ambient pressure. The fact that the sandstones used in this study were of a higher porosity and heated at elevated effective pressures means that thermal microcracking is unlikely to be the primary weakening mechanism. In addition, the BSE micrographs displayed in Appendix B and Figure B1 do not show any discernible difference between an undeformed sample of Bleursville sandstone and one which has been heated to 150°C while at an effective pressure of 10 MPa. In addition, while significant clay dehydroxylation is expected to occur at temperatures well above 150°C (Earnest, 1991). There is no evidence of any additional microcracking in or around the clay particles in heat-treated, undeformed Bleursville sandstone as shown in Appendix B and Figure B1.

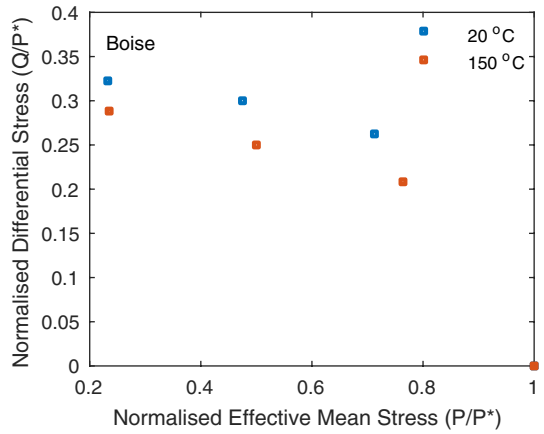

Figure 15. The yield envelope of Boise sandstone with the values of both differential stress and effective mean stress normalized by the P^* stress value.

While our experimental evidence suggests that a reduction in fracture toughness has occurred, it is currently not possible to determine what component(s) of the sandstone are experiencing the weakening. Likewise, the experiments on Boise sandstone suggested that increased crack kinetics were observed, but again it is currently unclear at this stage where the increased rates of subcritical cracking occurred. Table 1 shows that in general Locharbriggs sandstone experienced the smallest percentage of weakening. This sandstone was also the sandstone with the highest percentage of quartz and the lowest amounts of feldspars and clays, which suggests that the higher quartz content may lower the weakening observed at high temperature. Nevertheless, even a sandstone of nearly pure quartz could be expected to show signs of weakening at elevated temperatures as experiments carried out on pure quartz sand by Karner et al. (2008) and Choens & Chester (2018) demonstrated that the value of P^* was reduced at 150°C by ~10%. These authors also explored the combined effect of strain rate and temperature and noticed that at lower strain rates the weakening effect of elevated temperature was greater and this was attributed to

an increase in subcritical cracking at lower strain rates. One additional unknown factor is the role of fluid chemistry in the weakening observed at elevated temperature; in quartz, salinity has been shown to decrease surface energy (Parks, 1984) and increase subcritical crack growth rate (Atkinson & Meredith, 1981), but the temperature dependence of those effects has not been systematically studied. The chemical composition of the fluid may have second order impact on toughness, but could become more significant at very low strain rates by controlling the rate of subcritical crack growth.

Overall, we interpret the weakening observed at elevated temperature in our data as a combination of a decrease in fracture toughness and, to some minor extent, an increase in subcritical crack growth rate. In any case, it is expected that subcritical crack growth becomes significant at lower strain rates, as demonstrated in the both the brittle and ductile regime in sandstones (e.g., Heap, Baud, Meredith, Bell, et al., 2009; Heap, Baud, & Meredith, 2009; Heap et al., 2015) and sand (Karner et al., 2008; Choens & Chester, 2018). Elevated temperatures would tend to increase the threshold strain rate below which subcritical crack growth becomes significant; this remains to be tested in detail in long-term creep tests.

8. Conclusion

In this study, we demonstrated through triaxial deformation experiments performed on water saturated samples of Bleursville, Locharbriggs, and Boisze sandstones, that increasing the temperature from room temperature to 150°C weakens sandstone by an non negligible amount in both the brittle and ductile regime. This weakening varies by rock type and the effective pressure used, but in general is more pronounced in the compactive ductile regime than in the brittle regime. The yield stress in the ductile regime was reduced by up to 33%, whereas in the brittle regime the maximum reduction observed was 18%. The lowering of the yield stress corresponds to a shrinking of the elliptical yield envelope. The overall weakening of the rocks with increasing temperature under hydrothermal conditions is interpreted as a reduction of fracture energy, possibly combined, to a minor extent, with an increase in the rate of subcritical cracking.

Our results on sandstones are consistent with observations on sand aggregates (e.g., Choens & Chester, 2018), and demonstrate that elevated temperature facilitates cataclastic compaction processes. With increasing depth in the crust, both confining pressure and temperature act to favor compactant deformation of sandstones: pressure tends to promote grain crushing and porosity reduction as opposed to dilatant crack opening, and temperature facilitates these cracking processes. Due to the thermal activation of subcritical cracking processes, we expect temperature to have an even greater weakening effect at low strain rates, which should be detectable in creep tests.

Appendix A: Variability in elastic behavior in Bleursville sandstone

Figure A1 presents the porosity change occurring as a consequence of hydrostatic loading from an effective pressure of 5 MPa–100 MPa for several experiments carried out on Bleursville sandstone at either room temperature or at 150°C. At room temperature the total porosity reduction at an effective pressure of 100 MPa is between ~1.2% and 1.5% and at 150°C the porosity reduction is between ~1.4% and 1.7%.

Figure A2 presents the Young's modulus calculated from the stress strain curve for every experiment in this study at both room temperature and 150°C. It can be seen that there is no systematic measurable change as a result of the temperature increase.

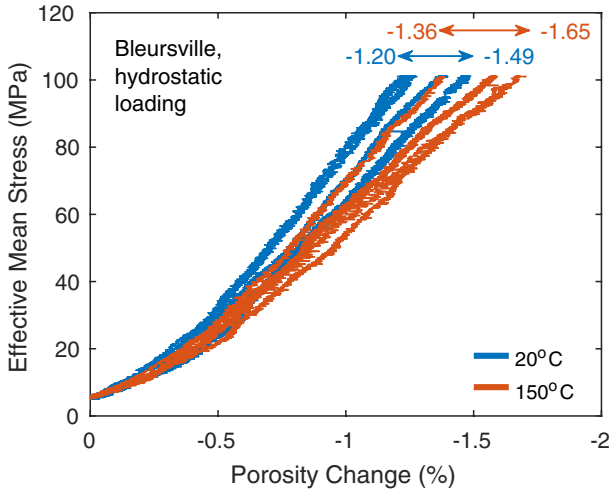

Figure A1. Porosity change as a function of effective mean stress for the hydrostatic loading of Bleursville sandstone from 10 to 100 MPa. Blue curves indicate room temperature tests and red curves represent experiments carried out at 150°C.

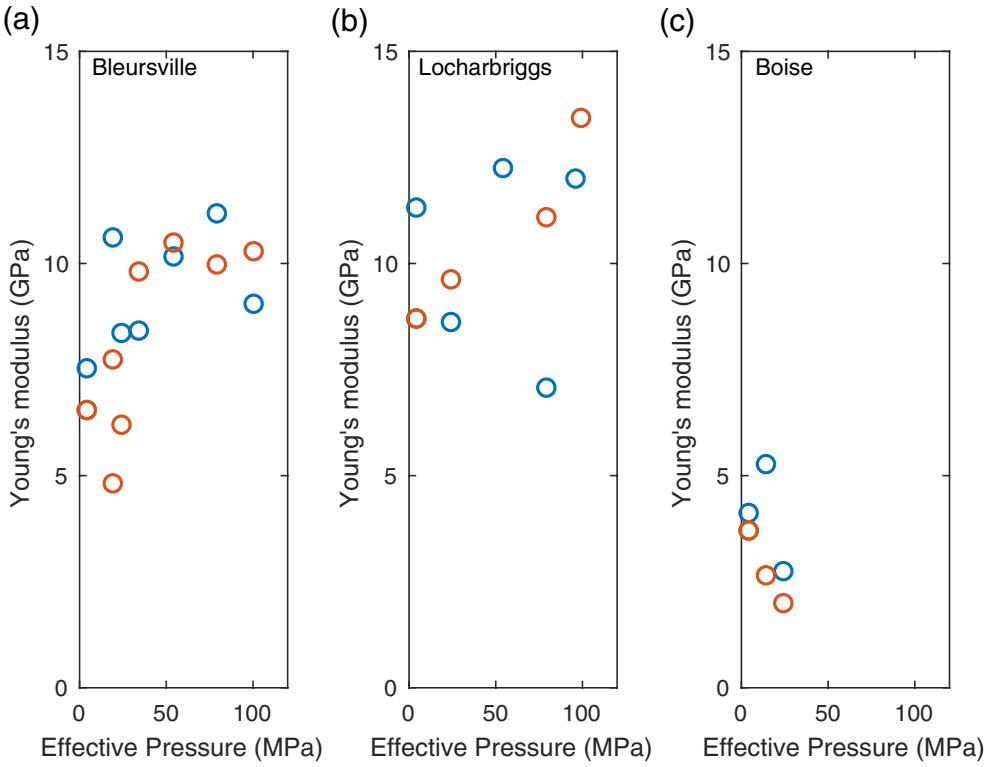

Figure A2. The Young's moduli for Bleursville, Locharbriggs and Boise sandstones as calculated from the gradient of the quasi-linear phase of the respective stress-strain curves, at a range of effective pressures while being deformed at room temperature (blue) or 150°C (red).

Appendix B: Additional Micrographs

Figure B1 shows BSE micrographs of an intact sample of Bleursville sandstone next to BSE micrographs from a sample of Bleursville sandstone heated to 150°C while at an effective pressure of 10 MPa. There appears to be no great difference between the two samples, and both just show a small number of intragranular cracks, which are either formed naturally or are induced during the coring procedure, and can therefore assumed to be relatively consistent between samples.

In Figures B2 and B3, BSE micrographs are shown of samples which are representative of the brittle and ductile regimes, at both deformation temperatures. Samples deformed at an effective pressure of 5 MPa, exhibit very localized deformation around a sample scale shear fracture. The samples deformed at an effective pressure of 35 MPa appear to be highly damaged in approximately one-third of the sample, and the remaining part of the samples are relatively undamaged.

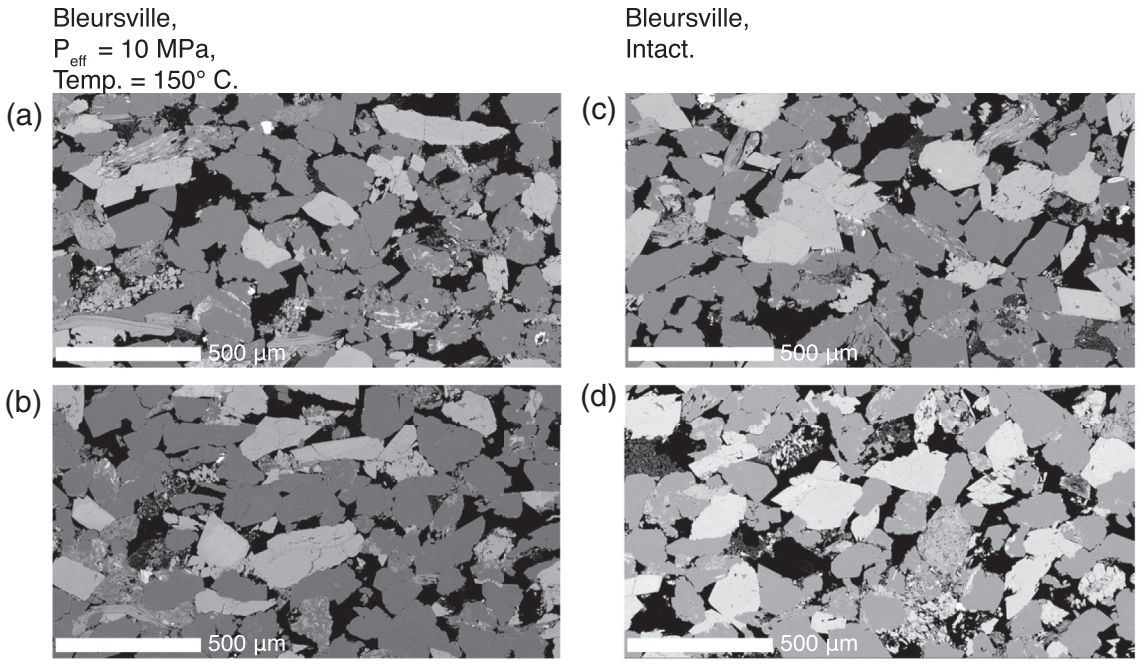

Figure B1. BSE micrographs (64 times zoom) of a Bleursville sandstone sample heated to 150°C while at an effective pressure of 10 MPa (a) and (b), and BSE micrographs (64 times zoom) of a Bleursville sandstone sample which has not experienced any additional pressure or temperature in the laboratory (c) and (d).

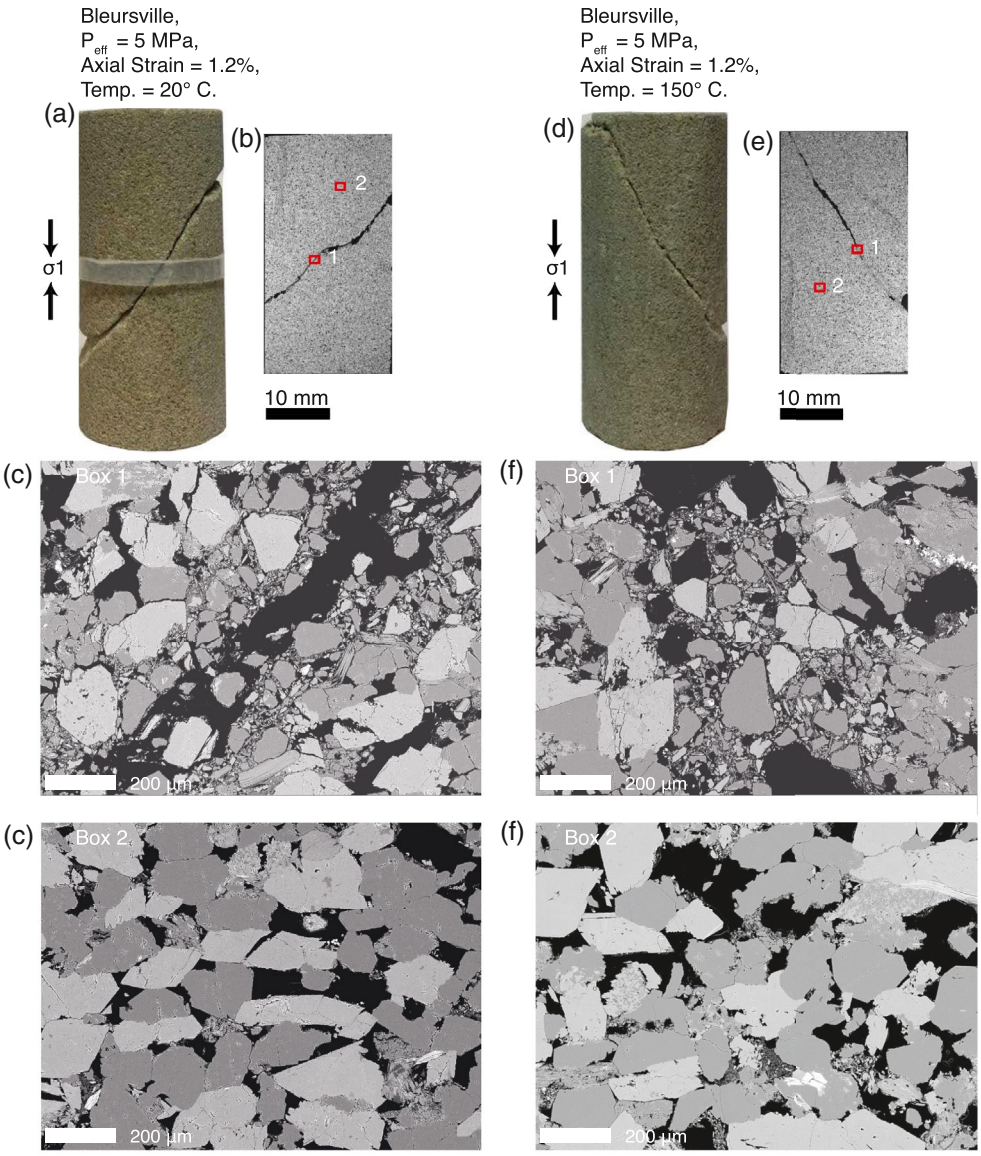

Figure B2. Bleursville sandstone samples deformed at $P_{\text{eff}} = 5$ MPa, and either room temperature (a, b and c) or 150°C (d, e, and f) to ~1.2% axial strain before failure. Included is a photo of the sample post deformation (a and d), a BSE scan (b and e) of nearly the whole sample (~40 mm of the 53 mm long sample is covered), a 100 times zoom of a highly damaged area, the location of which is indicated by red box numbered 1, and a 100 times zoom of a less damaged area, the location of which is indicated by a red box numbered 2. Note, the photo and the BSE scans are only aligned in the direction of compression and not necessarily on the viewing axis.

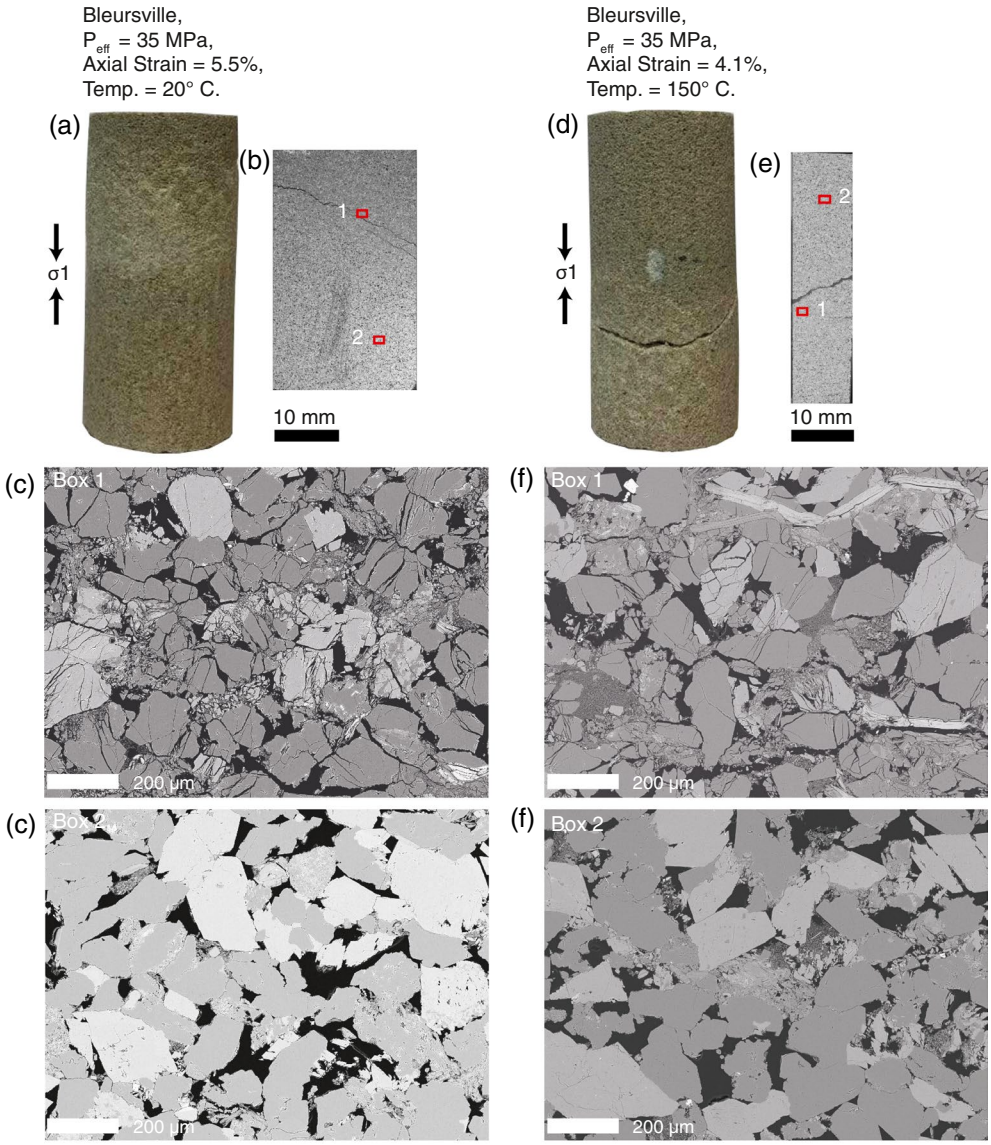

Figure B3. Bleursville sandstone samples deformed at P_{eff} = 35 MPa, and either room temperature (a, b and c) or 150°C (d, e, and f). The sample deformed at room temperature experienced 5.5% axial strain and the sample deformed at 150°C experienced 4.1% before the experiment was ended. Included is a BSE scan (b and e) of nearly the whole sample (~40 mm of the 53 mm long sample is covered), a 100 times zoom of a highly damaged area, the location of which is indicated by a red box numbered 1, and a 100 times zoom of a less damaged area, the location of which is indicated by a red box numbered 2. The sample scale scan of the 150°C sample only covers half the width of the sample. Note, the photo and the BSE scans are only aligned in the direction of compression and not necessarily on the viewing axis.

Data Availability Statement

The data related to this study may be found at the NGDC repository of the British Geological Survey (ID. 35125) www.bgs.ac.uk/services/ngdc/accessions/index.html?#item135125.

References

Anderson, O. L., & Grew, P. C. (1977). Stress corrosion theory of crack propagation with applications to geophysics. *Reviews of Geophysics and Space Physics*, *15*, 77–104.

Acknowledgments
The authors thank the associate editor and two anonymous reviewers for their constructive comments. Financial support was received from the UK Natural Environment Research Council (grants NE/L002485/1, NE/K009656/1 and NE/S000852/1). NB acknowledges support from the European Research Council under the European Union's Horizon 2020 research and innovation programme (project RockDEaF, grant agreement #804685). Discussions with Patrick Baud helped to shape this project. Neil Hughes, Steve Boon and Nic Snead contributed to the design and construction of the triaxial apparatus. Microstructural characterization was executed at the MINT facility of the research infrastructure EPOS-NL (https://epos-nl.nl/facilities/). EPOS-NL is funded by the Dutch Research Council (NWO).

Ashby, M. F., & Hallam, S. D. (1986). The failure of brittle solids containing small cracks under compressive stress states. *Acta Metallurgica*, *34*(3), 497–510.
Ashby, M. F., & Sammis, C. G. (1990). The damage mechanics of brittle solids in compression. *Pure and Applied Geophysics*, *133*(3), 489–521.
Atkinson, B. K. (1979). A fracture mechanics study of subcritical tensile cracking of quartz in wet environments. *Pure and Applied Geophysics*, *117*, 1011–1024.
Atkinson, B. K. (1984). Subcritical crack growth in geological materials. *Journal of Geophysical Research*, *89*(B6), 4077–4114.
Atkinson, B. K., & Meredith, P. G. (1981). Stress corrosion cracking of quartz: A note on the influence of chemical environment. *Tectonophysics*, *77*(1–2), T1–T11.
Aydin, A., & Johnson, A. M. (1983). Analysis of faulting in porous sandstones. *Journal of Structural Geology*, *5*(1), 19–31.
Balme, M. R., Rocchi, V., Jones, C., Sammonds, P. R., Meredith, P. G., & Boon, S. (2004). Fracture toughness measurements on igneous rocks using a high-pressure, high-temperature rock fracture mechanics cell. *Journal of Volcanology and Geothermal Research*, *132*(2–3), 159–172.
Baud, P., Meredith, P. G., & Townend, E. (2012). Permeability evolution during triaxial compaction of an anisotropic porous sandstone. *Journal of Geophysical Research*, *117*, B05203. https://doi.org/10.1029/2012JB009176
Baud, P., Reuschlé, T., Ji, Y., Cheung, C. S., & Wong, T.-F. (2015). Mechanical compaction and strain localization in Bleurswiller sandstone. *Journal of Geophysical Research*, *120*, 6501–6522. https://doi.org/10.1002/2015JB012192
Baud, P., Schubnel, A., & Wong, T.-F. (2000). Dilatancy, compaction, and failure mode in Solnhofen limestone. *Journal of Geophysical Research*, *105*(B8), 19289–19303.
Bemabe, Y., & Brace, W. (1990). Deformation and fracture of berea sandstone. In *The Brittle-Ductile Transition in Rocks, Geophysical Monograph Series* (Vol. *56*, pp. 91–101).
Bésuelle, P., Baud, P., & Wong, T.-F. (2003). Failure mode and spatial distribution of damage in rothbach sandstone in the brittle-ductile transition. In *Thermo-hydro-mechanical coupling in fractured rock* (pp. 851–868). Springer.
Blanpied, M. L., Lockner, D. A., & Byerlee, J. D. (1995). Frictional slip of granite at hydrothermal conditions. *Journal of Geophysical Research*, *100*(B7), 13045–13064.
Brantut, N., Baud, P., Heap, M., & Meredith, P. (2012). Micromechanics of brittle creep in rocks. *Journal of Geophysical Research: Solid Earth*, *117*(B8), B08412.
Brantut, N., Heap, M. J., Baud, P., & Meredith, P. G. (2014). Rate- and strain-dependent brittle deformation of rocks. *Journal of Geophysical Research*, *119*, 1818–1836. https://doi.org/10.1002/2013JB010448
Byerlee, J. D. (1978). Friction of rocks. *Pure and Applied Geophysics*, *116*, 615–626.
Chapman, D. S. (1986). Thermal gradients in the continental crust. In J. B. Dawson, D. A. Carswell, J. Hall, & K. H. Wedepohl (Eds.), *The nature of the lower continental crust* (Vol. 24, pp. 63–70). London: Geological Society.
Chester, F. M. (1994). Effects of temperature on friction: Constitutive equations and experiments with quartz gouge. *Journal of Geophysical Research*, *99*(B4), 7247–7261.
Choens, R. C., & Chester, F. M. (2018). Time-dependent consolidation in porous geomaterials at in situ conditions of temperature and pressure. *Journal of Geophysical Research*, *123*, 6424–6441. https://doi.org/10.1029/2017JB015097
Darot, M., & Guéguen, Y. (1986). Slow crack growth in minerals and rocks: Theory and experiments. *Pure and Applied Geophysics*, *124*(4/5), 677–692.
Darot, M., Guéguen, Y., Benchemam, Z., & Gaboriaud, R. (1985). Ductile-brittle transition investigated by micro-indentation: Results for quartz and olivine. *Physics of the Earth and Planetary Interiors*, *40*, 180–186.
Earnest, C. (1991). *Thermal analysis of selected illite and smectite clay minerals. Part I: Illite clay specimens*. Thermal analysis in the geosciences (pp. 270–286). Springer.
Feng, G., Kang, Y., Chen, F., Liu, Y.-w., & Wang, X.-c. (2018). The influence of temperatures on mixed-mode (i+ ii) and mode-ii fracture toughness of sandstone. *Engineering Fracture Mechanics*, *189*, 51–63.
Fortin, J., Schubnel, A., & Guéguen, Y. (2005). Elastic wave velocities and permeability evolution during compaction of bleurswiller sandstone. *International Journal of Rock Mechanics and Mining Sciences*, *42*(7–8), 873–889.
Fossen, H., Schulz, R. A., Shipton, Z. K., & Mair, K. (2007). Deformation bands in sandstone: A review. *Journal of the Geological Society*, *164*(4), 755–769.
Guéguen, Y., & Palciauskas, V. (1994). *Introduction to the physics of rocks*. Princeton, NJ: Princeton University Press.
Handin, J., Hager, R. V., Jr, Friedman, M., & Feather, J. N. (1963). Experimental deformation of sedimentary rocks under confining pressure: pore pressure tests. *AAPG Bulletin*, *47*(5), 717–755.
Hangx, S. J. T., & Brantut, N. (2019). Micromechanics of high-pressure compaction in granular quartz aggregates. *Journal of Geophysical Research*, *124*, 6560–6580. https://doi.org/10.1029/2018JB016494
Heap, M. J., Baud, P., & Meredith, P. G. (2009). Influence of temperature on brittle creep in sandstones. *Geophysical Research Letters*, *36*, L19305. https://doi.org/10.1029/2009GL039373
Heap, M. J., Baud, P., Meredith, P. G., Bell, A. F., & Main, I. G. (2009). Time-dependent brittle creep in Darley Dale sandstone. *Journal of Geophysical Research*, *114*, B07203. https://doi.org/10.1029/2008JB006212
Heap, M. J., Brantut, N., Baud, P., & Meredith, P. G. (2015). Time-dependent compaction band formation in sandstone. *Journal of Geophysical Research*, *120*, 4808–4830. https://doi.org/10.1002/2015JB012022
Jian-ping, Z., He-ping, X., Hong-wei, Z., & Su-ping, P. (2010). Sem in situ investigation on thermal cracking behaviour of pingdingshan sandstone at elevated temperatures. *Geophysical Journal International*, *181*(2), 593–603.
Karner, S. L., Kronenberg, A. K., Chester, F. M., Chester, J. S., & Hajash, A., Jr (2008). Hydrothermal deformation of granular quartz sand. *Journal of Geophysical Research*, *113*, B05404. https://doi.org/10.1029/2006JB004710
Lawn, B. R. (1993). *Fracture of brittle solids* (2nd ed.). Cambridge: Cambridge University Press.
Mair, K., Main, I., & Elphick, S. (2000). Sequential growth of deformation bands in the laboratory. *Journal of Structural Geology*, *22*(1), 25–42.
Maugis, D. (1985). Subcritical crack growth, surface energy, fracture toughness, stick-slip and embrittlement. *Journal of Materials Science*, *20*, 3041–3073.
Menéndez, B., Zhu, W., & Wong, T.-F. (1996). Micromechanics of brittle faulting and cataclastic flow in Brea sandstone. *Journal of Structural Geology*, *18*(1), 1–16.
Meredith, P. G., & Atkinson, B. K. (1985). Fracture toughness and subcritical crack growth during high-temperature tensile deformation of Westerly granite and Black gabbro. *Physics of the Earth and Planetary Interiors*, *39*, 33–51.

Mollema, P. N., & Antonellini, M. A. (1996). Compaction bands: A structural analog for anti-mode I cracks in Aeolian sandstone. *Tectonophysics*, *267*(1–4), 209–228.
Nemat-Nasser, S., & Horii, H. (1982). Compression-induced nonplanar crack extension with application to splitting, exfoliation, and rockburst. *Journal of Geophysical Research*, *87*(B8), 6805–6821.
Niemeijer, A. R., Spiers, C. J., & Bos, B. (2002). Compaction creep of quartz sand at 400–600°C: Experimental evidence for dissolution-controlled pressure solution. *Earth and Planetary Science Letters*, *195*, 261–275.
Parks, G. A. (1984). Surface and interfacial free energies of quartz. *Journal of Geophysical Research*, *89*(B6), 3997–4008.
Reviron, N., Reuschlé, T., & Bernard, J.-D. (2009). The brittle deformation regime of water-saturated siliceous sandstones. *Geophysical Journal International*, *178*(3), 1766–1778.
Rice, J. R. (1978). Thermodynamics of the quasi-static growth of Griffith cracks. *Journal of the Mechanics and Physics of Solids*, *26*, 61–78.
Rutter, E. H. (1976). The kinetics of rock deformation by pressure solution. *Philosophical Transactions of the Royal Society of London,Series A*, *283*(1312), 203–219.
Sammis, C. G., & Ashby, M. F. (1986). The failure of brittle porous solids under compressive stress states. *Acta Metallurgica*, *34*(3), 511–526.
Sternlof, K. R., Karimi-Fard, M., Pollard, D. D., & Durlofsky, L. J. (2006). Flow and transport effects of compaction bands in sandstone at scales relevant to aquifer and reservoir management. *Water Resources Research*, *42*, W07425. https://doi.org/10.1029/2005WR004664
Teufel, L. W., Rhett, D. W., & Farrell, H. E. (1991). Effect of reservoir depletion and pore pressure drawdown on in situ stress and deformation in the Ekofisk field, North Sea. Paper presented at 32nd U.S. symposium on rock mechanics American Rock Mechanics Association.
Wan, K.-T., Lathabai, S., & Lawn, B. R. (1990). Crack velocity functions and thresholds in brittle solids. *Journal of the European Ceramic Society*, *6*, 259–268.
Wong, T.-F. (1990). A note on the propagation behavior of a crack nucleated by a dislocation pileup. *Journal of Geophysical Research*, *95*(B6), 8639–8646.
Wong, T.-F., & Baud, P. (2012). The brittle-ductile transition in porous rock: A review. *Journal of Structural Geology*, *44*, 25–53.
Wong, T.-F., Ko, S.-C., & Olgaard, D. L. (1997). Generation and maintenance of pore pressure excess in a dehydrating system 2. theoretical analysis. *Journal of Geophysical Research*, *102*(B1), 841–852.
Wu, X. Y., Baud, P., & Wong, T.-F. (2000). Micromechanics of compressive failure and spatial evolution of anisotropic damage in Darley Dale sandstone. *International Journal of Rock Mechanics and Mining Sciences*, *37*, 143–160.
Zhang, X., Spiers, C. J., & Peach, C. J. (2010). Compaction creep of wet granular calcite by pressure solution at 28°C to 150°C. *Journal of Geophysical Research*, *115*, B09217. https://doi.org/10.1029/2008JB005853
Zhang, J., Wong, T.-F., & Davis, D. M. (1990). Micromechanics of pressure-induced grain crushing in porous rocks. *Journal of Geophysical Research*, *95*(B1), 341–351.
Zhu, W., & Wong, T.-F. (1997). The transition from brittle faulting to cataclastic flow: Permeability evolution. *Journal of Geophysical Research*, *102*(B2), 3027–3041.